Ferromagnetic Exchange through Unoccupied Bridging Ligand Orbitals. Optical Spectroscopic Investigation of μ-1,1-Azido Copper(II) Dimers†

Ingo von Seggern,‡ Felix Tuczek,*,‡ and Wolfgang Bensch§

Institut für Anorganische und Analytische Chemie, Johannes Gutenberg Universität Mainz, Staudingerweg 9, D-55099 Mainz, Germany, and Anorganische Chemie I, Johann Wolfgang von Goethe Universität Frankfurt, Marie-Curie-Strasse 11, D-60439 Frankfurt, Germany

Received March 14, 1995⊗

The azide $(\pi^{nb})_\sigma \rightarrow$ Cu charge transfer (CT) spectra of two Cu(II) μ-1,1-azido dimers, $[Cu_2(tmen)_2(N_3)(OH)](ClO_4)_2$ (tmen = tetramethylethylenediamine) and $[Cu_2(tbupy)_4(N_3)_2](ClO_4)_2$ (tbupy = *tert*-butylpyridine), are recorded by solution and single-crystal polarized absorption spectroscopy. The spectra are interpreted with a valence bond configuration interaction (VBCI) model. This model parametrizes antiferromagnetic and ferromagnetic interactions present in the manifold of CT states in terms of transfer integrals between the metal d orbitals and the highest occupied MO of azide, $(\pi^{nb})_\sigma$, and the lowest unoccupied orbital of azide, $(\pi^*)_\sigma$. These two transfer integrals are found to be approximately equal, leading to a compensation of ferro- and antiferromagnetic interactions in the CT state, which in turn is the reason for the observed ferromagnetic coupling in the ground state. The origin of the ferromagnetic interaction is a polarization of the unpaired metal electrons by an unpaired electron in the azide $(\pi^*)_\sigma$ orbital in a ligand excited (LE) state. The spin polarization model (Charlot, M.-F.; Kahn, O.; Chaillet, M.; Larrieu, C. *J. Am. Chem. Soc.* **1986,** *108,* 2574) is found to be a spin-Hamiltonian description of this ferromagnetic interaction through the azide π^* orbital. In terms of a molecular orbital description, the combined interaction of azide $(\pi^{nb})_\sigma$ and $(\pi^*)_\sigma$ orbitals drive the μ-1,1 systems toward accidental degeneracy between HOMO and LUMO, the condition for ferromagnetic coupling in the "active electron approximation".

I. Introduction

The search for ferromagnetic molecular materials has renewed the interest in mechanisms potentially leading to ferromagnetic coupling between molecular building blocks.[1−5] With respect to the interaction between identical transition metal centers via closed-shell bridges, there are so far two generally accepted concepts of ferromagnetic coupling, i.e. (a) bridging via orthogonal magnetic orbitals and (b) accidental degeneracy of the HOMO and the LUMO.[1,5] The latter mechanism has been traditionally invoked in the framework of the "active electron approximation" [6a] to explain the ferromagnetic interaction in bis(μ-hydroxo) Cu(II) dimers with a Cu−O−Cu angle Φ close to 95°.[6b] Strong ferromagnetic interaction is also found in μ-1,1-azide-bridged Cu(II)[7−9] and Ni(II)[10] dimers. Remarkably, the same ligand mediates strongly *antiferromagnetic* dimer coupling in the cis μ-1,3 bridging geometry.[11−13] Similar observations have been made with bridging ligands like thiocyanate and cyanate.[14] Kahn et al. have presented a phenomenological description of these findings based on the "spin polarization" effect and formulated a corresponding spin-Hamiltonian explaining qualitatively the differences in magnetic behavior between the cis-μ-1,3 and the μ-1,1 Cu(II) dimers.[15] However, it is still under debate whether this "spin polarization model" in fact describes the major part of the ferromagnetic coupling in μ-1,1-azide compounds or whether these systems just represent another case of accidental degeneracy of HOMO and LUMO like the μ-OH dimers with $\Phi \approx 95°$.[16] On the other hand, the μ-1,1 bridging azide ligand seems to have a "special" tendency to mediate ferromagnetic coupling since most of the known μ-1,1-azide-bridged Cu(II) and Ni(II) dimers are ferromagnetically coupled and, for equal bridging angles in bis(μ-1,1 azide) and bis(μ-hydroxo) Cu(II) dimers, the coupling is *ferromagnetic* in the azide and *antiferromagnetic* in the hydroxo case.[17] So far, the spin polarization model is the only rationalization of this special ability of the azide group, including

* Author to whom correspondence should be addressed.

† Presented in part at the 2nd meeting of the European Network on Magnetic Molecular Materials, Valencia, Spain, Feb 18−22, 1995.

‡ Johannes Gutenberg Universität.

§ Johann Wolfgang von Goethe Universität.

⊗ Abstract published in *Advance ACS Abstracts,* October 1, 1995.

(1) Kahn, O. *Molecular Magnetism*; VCH Publishers: Weinheim, New York, 1993.
(2) Kollmar, C.; Kahn, O. *Acc. Chem. Res.* **1993**, *26*, 259.
(3) *Magnetic Molecular Materials*; Gatteschi, D., Kahn, O., Miller, J. S., Palacio, F., Eds.; NATO ASI Series; Kluwer Academic Publishers: Dordrecht, 1991.
(4) Miller, J. S.; Epstein, A. J.; Reiff, W. M. *Chem. Rev.* **1988**, *88*, 201.
(5) *Magneto Structural Correlations in Exchange Coupled Systems*; Willett, R. D., Gatteschi, D., Kahn, O., Eds.; NATO ASI Series; Reidel: Dordrecht, 1985.
(6) (a) Kahn, O., in ref 5, pp 37−56. (b) Hatfield, W. E., in 555−602.
(7) Comarmond, J.; Plumeré, P.; Lehn, J.-M.; Agnus, Y.; Louis, R.; Weiss, R.; Kahn, O.; Morgenstern-Badarau, I. *J. Am. Chem. Soc.* **1982**, *104*, 6330.
(8) Kahn, O.; Sikorav, S.; Gouteron, J.; Jeannin, S.; Jeannin, Y. *Inorg. Chem.* **1983**, *22*, 2877.
(9) Sikorav, S.; Bkouche-Waksman, I.; Kahn, O. *Inorg. Chem.* **1984**, *23*, 490.
(10) Vicente, R.; Escuer, A.; Ribas, J.; Salah el Fallah, M.; Solans, X.; Font-Bardia, M. *Inorg. Chem.* **1993**, *32*, 1920 and references therein.
(11) McKee, V.; Zvagulis, M.; Dagdigian, J. V.; Patch, M. G.; Reed, C. R. *J. Am. Chem. Soc.* **1984**, *106*, 4765.
(12) Sorrell, T. N.; O'Connor, C. J.; Anderson, O. P.; Reibenspies, J. H. *J. Am. Chem. Soc.* **1985**, *107*, 4199.
(13) Tuczek, F.; Bensch, W. *Inorg. Chem.* **1995**, *34*, 1482.
(14) Arriortua, M. I.; Cortès, R.; Mesa, J. L.; Lezama, L.; Rojo, T.; Villeneuve, G. *Transition Met. Chem.* **1987**, *13*, 371.
(15) Charlot, M.-F.; Kahn, O.; Chaillet, M.; Larrieu, C. *J. Am. Chem. Soc.* **1986**, *108*, 2574.
(16) See, e.g.; Vicente, R.; Escuer, A.; Ribas, J.; Salah el Fallah, M.; Solans, X.; Font-Bardia, M. *Inorg. Chem.* **1993**, *32*, 1920.
(17) The bis(μ-hydroxo) complex $[Cu(dmaep)(OH)]_2(ClO_4)_2$ has a Cu−O−Cu angle of 100.4° and a $2J$ value of -200 cm^{-1}: Lewis, D. L.; McGregor, K. T.; Hatfield, W. E.; Hodgson, D. J. *Inorg. Chem.* **1974**, *13*, 1013. The bis(μ-1,1-azido) complex $[Cu(tbupy)_2(N_3)]_2(ClO_4)_2$ (**2**) has a Cu−N−Cu angle of 100.5° and a $2J$ value of $+105 \pm 20$ cm^{-1} (see text).

0020-1669/95/1334-5530$09.00/0

Scheme 1

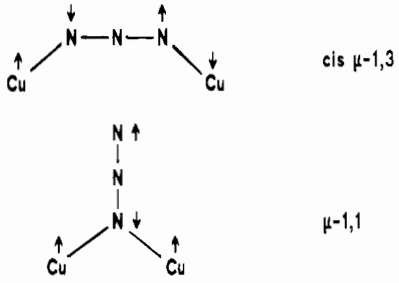

the striking magnetostructural correlation between the cis-μ-1,3- and the μ-1,1-bridged dimers. In terms of this model, the key property of the azide group is a "polarization" of the two spins in the highest occupied orbital at opposite nitrogen atoms of the N_3^- group (Scheme 1). Coupling in a cis μ-1,3 fashion supposedly proceeds via *individual* pairing of the Cu spins with the (e.g. β) azide spin at the "left" N atom and the α spin at the "right" N atom (or vice versa) and, hence, necessarily leads to *antiferromagnetic* coupling whereas bridging in a μ-1,1 fashion is thought to lead to a *simultaneous* pairing of the two (e.g. α) Cu spins with the β spin on the bridging N atom (or vice versa) and, hence, a *ferromagnetic* coupling between the two copper spins. It is, however, not obvious how these ideas are related to more common descriptions of magnetic exchange in terms configuration interaction in a VB (Anderson theory)[18] or molecular orbital framework ("active electron approximation" and beyond[19]).

Starting from the interpretation of the CT spectra of antiferromagnetically coupled Cu peroxo and azide dimers of biological relevance, we recently formulated a so-called VBCI model which correlates the CT excited state spectral features of bridged dimers with their ground state magnetic properties.[20-22] On the basis of his concept, bridging ligand $\rightarrow$ Cu CT transitions have been used to experimentally probe the individual superexchange pathways leading to the observed antiferromagnetic coupling in the ground state. Two key properties of the CT spectrum in this respect are (a) the splitting of a particular CT transition and (b) the overall shift of a CT transition to lower energy upon going from the monomer to the dimer. Here, "monomer" means one, e.g. Cu, center coordinated to the ligand of interest, e.g. peroxide or azide, in the same fashion as in the "dimer" where two Cu units are bridged by the same ligand. It has been shown that the dimer splitting of a LMCT transition is related to the HOMO−LUMO splitting of the complex which is also the key quantity in theories of magnetic coupling in dimers within the "active-electron approximation".[6a,23] The low-energy shift of the CT transition(s), on the other hand, is due to a strongly antiferromagnetic interaction in the CT excited state between the unpaired electron in the bridging ligand orbital and the unpaired electron in the highest energy Cu d orbital having large overlap.[24] This "excited-state antiferromagnetism" (ESAF) is the origin of ground state antiferromagnetism (GSAF) due to mixing between the zeroth-order ground and CT excited states. Within the VBCI model, ESAF is treated by configuration interaction with the metal-to-metal CT (MMCT) and double CT (DCT) states. As this model is essentially a description of superexchange in antiferromagnetically coupled dimers, the question arises as to how these concepts work for *ferromagnetically* coupled systems like the μ-1,1-azide-bridged Cu(II) dimers. Specifically, the observed ground state ferromagnetism (GSF) should now be due to excited state ferromagnetism (ESF) like GSAF to ESAF in the antiferromagnetically coupled systems. The experimental test of this supposition is the first aim of this paper. To this end, we study the azide $\rightarrow$ Cu CT spectra of two μ-1,1-azide bridged binuclear Cu(II) systems, *viz.* $[Cu_2(tmen)_2(N_3)(OH)](ClO_4)_2$ (**1**) and $[Cu_2(tbupy)_4(N_3)_2](ClO_4)_2$ (**2**) by solution and single-crystal polarized absorption spectroscopy (tmen = tetramethylethylenediamine and tbupy = *tert*-butylpyridine). Both dimers are strongly ferromagnetically coupled with $2J > +200$ cm^{-1} for **1**[8] and $2J = +105$ cm^{-1} for **2**.[9]

The second goal of this paper is the theoretical interpretation of the observed CT excited state level structure. For ESF, there must be (at least) one strong ferromagnetic interaction that is able to overcome the strong antiferromagnetic contributions mentioned above (MMCT, DCT) which are always present in bridged dimers, regardless of the binding geometry of the bridging ligand. However, the set of three orbitals used so far in the VBCI description of bridged dimers, i.e. the doubly occupied bridging ligand HOMO and the two highest energy, singly occupied Cu d orbitals, is not sufficient to provide for this mechanism since all possible configurations have already been taken into account in the treatment. For the azide-bridged systems, we therefore also incorporate the LUMO of the ligand, i.e. the lowest unoccupied π^* orbital of the azide group. Spectroscopic results and calculations indicate that this orbital is 5.4 eV above the azide HOMO.[25] On the basis of the set of four orbitals $(\pi^{nb})_\sigma(N_3)$, $\pi^*_\sigma(N_3)$ and the two Cu d orbitals d_A and d_B, the VBCI model is developed in section IV for mono- and bis(μ-1,1-azide)-bridged dimers, and the consequences with respect to ferromagnetic coupling via the π^* orbital are considered. The optical solution and polarized single-crystal spectra of the two prototype Cu μ-1,1-azide dimers **1** and **2** are analyzed in section III and then parametrized in terms of this VBCI model in section V. In section VI, the VBCI description of the ferromagnetic interaction is interpreted as a polarization of the unpaired metal electrons by a single electron in the ligand π^* orbital, which closely resembles the "spin polarization" model. In fact, the corresponding Hamiltonian is shown to be a spin-Hamiltonian description of this ferromagnetic interaction via the azide π^* orbital. Finally, these concepts are related to the molecular orbital description of magnetic exchange within the active electron approximation.

II. Experimental Section

A. $[Cu_2(tmen)(\mu\text{-}N_3)(\mu\text{-}OH)](ClO_4)_2$ (tmen). This binuclear, μ-1,1-azide-bridged Cu(II) complex was first synthesized and structurally characterized by Kahn et al.[8] It crystallizes in the tetragonal space group $P4_2/mnm$ with 2 molecules per unit cell. In a slight modification of the literature procedure, 370.5 mg (1.0 mmol) of $Cu(ClO_4)_2 \cdot 6H_2O$ was dissolved in 10 mL of water, and 116.0 mg (1.0 mmol) of *N,N,N′,N′*-tetramethylethylenediamine (tmen) and 32.5 mg (0.5 mmol) of NaN_3 dissolved in 2.5 mL of water were added dropwise. (In the procedure of Kahn et al., 1.0 mmol of NaN_3 was used for the preparation, which was found to lead primarily to $[Cu(tmen)(N_3)_2]_2$.) Dark blue, almost black, well-formed quadratic platelets with dimensions up to several millimeters appeared after slow evaporation of the

(18) Anderson, P. W. *Solid State Phys.* **1963**, *14*, 99−214.
(19) de Loth, P.; Cassoux, P.; Daudey, J. P.; Malrieu, J. P. *J. Am. Chem. Soc.* **1981**, *103*, 4007.
(20) Tuczek, F.; Solomon, E. I. *Inorg. Chem.* **1993**, *32*, 2850.
(21) Tuczek, F.; Solomon, E. I. *J. Am. Chem. Soc.* **1994**, *116*, 6916.
(22) Solomon, E. I.; Tuczek, F.; Brown, C.; Root, D. *Chem. Rev.* **1994**, *94*, 827.
(23) Hay, P. J.; Thibeault, J. C.; Hoffmann, R. *J. Am. Chem. Soc.* **1975**, *97*, 4884.
(24) Desjardins, S. R.; Wilcox, D. E.; Musselman, R. L.; Solomon, E. I. *Inorg. Chem.* **1987**, *26*, 288.
(25) For an overview of experimental results and an SCF calculation, see: Fischer, C. R.; Kemmey, P. J.; Klemperer, W. G. *Chem. Phys. Lett.* **1977**, *47*, 545.

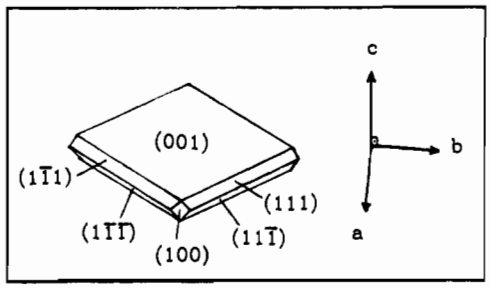

Figure 1. Morphology of $[Cu_2(tmen)_2(N_3)(OH)](ClO_4)$.

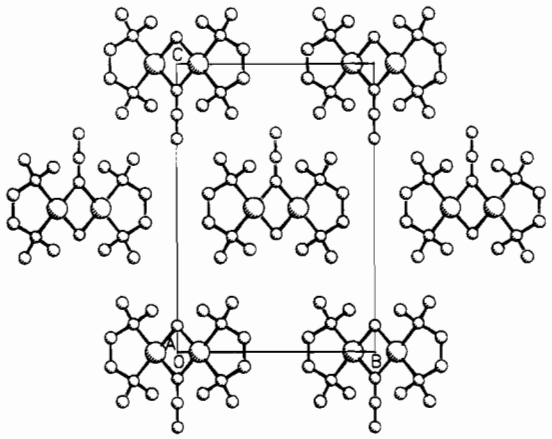

Figure 2. (100) projection of $[Cu_2(tmen)_2(N_3)(OH)](ClO_4)_2$.

solvent (~3 weeks). Thin platelets appeared violet in transmission. The identity of the product was checked with elemental analysis and X-ray powder diffractometry. The morphology of the crystals is displayed in Figure 1. The prominent face of the crystals is (001) and allows only the α spectrum with the *k* vector of the light parallel to *c* to be recorded. In order to obtain the π and σ spectra, respectively, a (100) face containing the *c* axis was prepared by a special grinding/polishing technique.[26] This plane was found to be dichroic under polarized light with **E** parallel to *c* intense blue and **E** perpendicular to *c* violet (as for the (001) face). Figure 2 gives the (100) projection of $[Cu_2(tmen)(\mu\text{-}N_3)(\mu\text{-}OH)](ClO_4)_2$ and shows that the azide groups are collinear with the *c* axis of the crystal and that the Cu−Cu vector is perpendicular to *c*. The complex is soluble in most polar solvents like water, ethanol, methanol, DMF, acetone, acetonitrile, dichloromethane, and chloroform. However, it is found by absorption measurements that it keeps its dimeric form only in chloroform, decaying into monomers in the other solvents.

B. $[Cu_2(tbupy)_4(\mu\text{-}N_3)_2](ClO_4)_2$ (tbupy). This binuclear, bis(μ-1,1-azide)-bridged Cu(II) complex was first synthesized and structurally characterized by Sikorav et al.[9] It crystallizes in the monoclinic space group $P2_1/c$ with 2 molecules per unit cell. Again, the literature procedure for the preparation of this complex was slightly modified in order to obtain large single crystals. Thus, 925 mg (2.5 mmol) of $Cu(ClO_4)_2{\cdot}6H_2O$ was dissolved in 100 mL of ethanol, and 875 mg (6.25 mmol) of *tert*-butylpyridine (tbupy) dissolved in 20 mL of EtOH, 81 mg of NaN_3 (1.25 mmol) dissolved in 2 mL of H_2O and 20 mL of EtOH were added dropwise. In the literature procedure, solid NaN_3 was added in stoichiometric amounts (2.5 mmol), which was found to lead to a brown insoluble precipitate, presumably, a polymeric Cu−tbupy−azide species. Hence, only half of the stoichiometric amount of NaN_3 was slowly added in a dilute form, causing a color change of the solution from blue-green to green-yellow. The clear solution was left 3 weeks at room temperature, leading to the formation of blue, almost black, rhombic (almost quadratic) platelets of dimensions up to 3 × 3 × 1 mm. Thin platelets appeared violet in transmission but were markedly dichroic under polarized light (brown−blue; *vide infra*). From the mother liquor were isolated violet-blue crystals of $[Cu(tbupy)_4](ClO_4)_2$ (*vide infra*). The identity of the binuclear azide complex was checked by elemental analysis and X-ray powder diffraction. The

(26) Tuczek, F.; Solomon, E. I. *Inorg. Chem.* **1992**, *31*, 945.

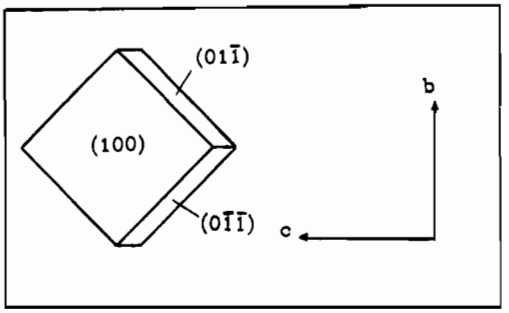

Figure 3. Morphology of $[Cu_2(tbupy)_4(N_3)_2](ClO_4)_2$.

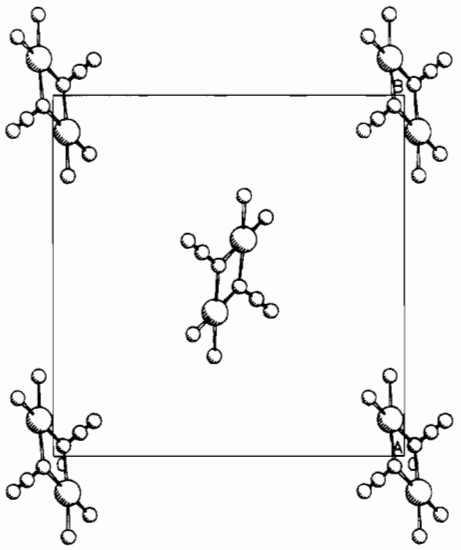

Figure 4. (100) projection of $[Cu_2(tbupy)_4(N_3)_2](ClO_4)_2$.

morphology of the crystals is displayed in Figure 3. The dominant, almost quadratic plane is (100). For **E** || *b*, the crystal appears brown and absorbs strongly whereas, for **E** || *c*, it appears blue and absorption is weak. Figure 4 gives the (100) projection of $[Cu_2(tbupy)_4(\mu\text{-}N_3)_2](ClO_4)_2$ and shows that the crystal spectra along *b* and *c* both contain contributions from the molecular *x* (along Cu−Cu), *y* (along the azide groups), and *z* polarizations. This point is further considered in section IIIB. The second face allowing polarized transmission measurements, i.e. (001), is not developed. The compound dissolves in ethanol, methanol, acetone, acetonitrile, chloroform, and toluene but not in water. Absorption measurements indicate that it decays into monomers in ethanol and acetonitrile whereas it remains intact in chloroform and toluene.

C. $[Cu(tbupy)_4](ClO_4)_2$. This monomeric complex was found as a byproduct in the preparation of the bis(μ-1,1-azide)-bridged dimer (*vide supra*). It can also be prepared by adding 540 mg (4.0 mmol) of *tert*-butylpyridine (tbupy) dissolved in 10 mL of ethanol to 370.5 mg (1.0 mmol) of $Cu(ClO_4)_2{\cdot}6H_2O$ in 30 mL ethanol under stirring. The intensely blue-violet solution was left for ~1 week to evaporate slowly at room temperature, leading to well-formed, rhombic platelets of the product. The identity of the product was checked by elemental analysis (%C found 53.16, calc 53.83; %H found 6.67, calc 6.525; %N found 6.91, calc 6.975). It was found that the dominant rhombic face of the crystals is (100), with the long diagonal axis being the *c* axis and the short diagonal axis the *b* axis. This face appears violet-blue in transmission with a weak dichroism; i.e., for **E** || *b* the crystal absorbs more strongly than for **E** || *c*. The crystal structure of the compound was determined by single-crystal X-ray diffraction; relevant structural parameters of this system are summarized in Table 1. Whereas the copper coordination in the dimeric tmen and tbupy systems A and B is quadratic-planar, the $O(ClO_4^-)$−Cu distances in the monomer are so short that they effectively participate in Cu coordination which therefore has to be described as distorted octahedral (with the perchlorate oxygens in axial positions) rather than quadratic-planar.

D. Measurements. All optical absorption measurements were carried out in a Bruins Omega-10 UV/vis/near-IR two-beam spectrom-

Table 1. Structural Data for $[Cu(tbupy)_4](ClO_4)_2$

space group	$P2_1/c$
molecules/unit cell	$Z = 2$
mol wt	803.28
density	1.194 g/cm^3
lattice constants	$a = 11.632(2)$ Å
	$b = 11.355(2)$ Å
	$c = 16.570(3)$ Å
	$\alpha = \gamma = 90°$
	$\beta = 96.57(3)°$
interatomic distances	Cu−N$_1$(tbupy) = 2.040(2) Å
	Cu−O(ClO$^-$) = 2.522(1) Å
bond angle	N$_2$(tbupy)−Cu−N$_2$(tbupy) = 92.18°

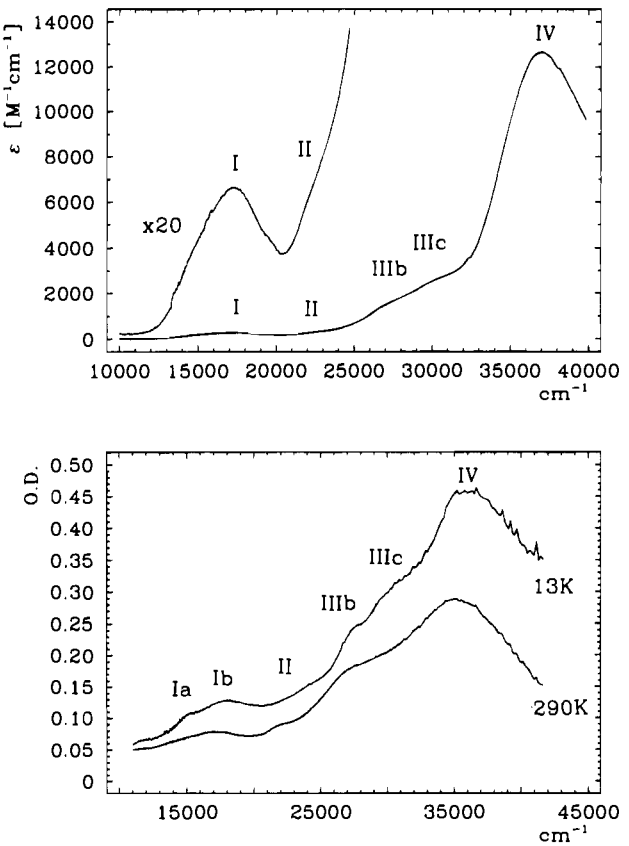

Figure 5. (a) Top: Chloroform solution spectrum of $[Cu_2(tmen)_2(N_3)(OH)](ClO_4)_2$. (b) Bottom: Nujol mull spectra of $[Cu_2(tmen)_2(N_3)(OH)](ClO_4)_2$ at 13 and 290 K.

eter equipped with a matched pair of Glan−Taylor polarizers and a flow-tube for temperature-dependent measurements down to liquid helium temperature. Single-crystal samples of thicknesses down to 6 μm were oriented under a polarizing microscope. The indexing of the crystals was performed using a four-circle diffractometer. The X-ray structure determination of $[Cu(tbupy)_4](ClO_4)_2$ was carried out with a STOE AED II diffractometer with graphite-monochromated Mo Kα radiation. The structure was solved and refined with the program package SHELX TL plus.

III. Spectroscopic Results and Spectral Analysis

A. tmen. Figure 5 displays the optical absorption spectra of $[Cu_2(tmen)_2(N_3)(OH)](ClO_4)_2$ dissolved in chloroform at room temperature (Figure 5a) and as a Nujol mull at 290 and 13 K, respectively (Figure 5b). In both the solution and solid-state spectra, five bands can be distinguished whose positions are given in Table 2. In the ligand field absorption region, band I is observed at 17 000 cm^{-1} in the solution spectrum ($\epsilon \approx 280$ M^{-1} cm^{-1}) and splits into band Ia at 15 500 cm^{-1} and band Ib at 18 000 cm^{-1} at low temperature. In the charge transfer (CT) absorption region, three bands are observed, a low-intensity band II at 22 000 cm^{-1} ($\epsilon \approx 250$ in solution) and two higher intensity bands IIIb at 27 500 cm^{-1} ($\epsilon \approx 1700$) and IIIc at 30 000 cm^{-1} ($\epsilon \approx 2500$); the last two, however, do not appear split in the 290 K Nujol spectrum. Finally, a high-energy, high-intensity band, band IV, is observed at 37 000 cm^{-1} ($\epsilon \approx 12\,600$ in solution).

In the context of this work, bands II and III are most interesting as they are possible candidates for azide → Cu CT transitions (see below). In particular, the splitting of band III needs to be explained. To this end, temperature-dependent single-crystal polarized absorption spectra of $[Cu_2(tmen)_2(N_3)(OH)](ClO_4)_2$ were recorded, which are displayed in Figure 6. Figure 6a shows the α spectra corresponding to molecular xy polarizations where x is along the Cu−Cu vector and y perpendicular to the molecular plane (cf. Figure 2). Again, bands I−III can be identified with the splitting of band I into Ia and Ib observable at low temperatures (cf. Table 2). Remarkably, the intensity of band II is strongly temperature dependent and drops to 0 at 32 K (see inset of Figure 6a). Further, the low-energy slope of band III shifts to higher energy upon lowering the temperature, leading to an almost separated band IIIb at 27 600 cm^{-1} ($\epsilon \approx 400$ at 32 K). In Figure 6b, the corresponding σ spectrum is displayed. Note that, in terms of electric dipole selection rules, σ corresponds to α, i.e. **E** || xy. The difference between the α and σ spectra lies in the orientation of the **H** vector relative to the crystal (molecular) axes; i.e., for α, **H** || ab (xy) and, for σ, **H** || c (z). Since magnetic dipole transitions are orders of magnitude less intense than electric dipole transitions, the difference between α and σ spectra is expected to be small. In fact, the σ spectrum is qualitatively similar to the α spectrum; in particular, the same intensity decrease of band II is observed as in the α spectrum. However, band Ib at 18 000 cm^{-1} is less intense in the σ than in the α spectrum, which allows a second band IIa at 19 600 cm^{-1} to be observed exhibiting an intensity decrease at low temperatures similar to that of band II. In the π spectrum (Figure 6c), finally, band II is much less intense. Since the π spectrum is polarized along z, this indicates band II is xy polarized. In addition, there appears a shoulder at ~25 000 cm^{-1} (band IIIa) decreasing rapidly in intensity upon cooling of the sample. At 32 K, this shoulder has a small, but nonvanishing, intensity which is clearly seen, as between band IIIb and band I (i.e. in the region of band II) the absorbance drops to zero. In the σ and α spectra (Figure 6a,b), there is some background under band II; however, the shoulder IIIa at the beginning of the low-energy slope of band III can also be observed in these spectra at low temperatures. In Figure 7, the 32 K α, σ, and π spectra are displayed again for comparison, and it is seen that the π spectrum between 24 000 and 27 000 cm^{-1} (bold) corresponds to the $\sigma(\alpha)$ spectra shifted by 400 cm^{-1} to lower energy. In particular, band IIIa appears at 24 800 cm^{-1} in the π and 25 200 cm^{-1} in the σ and α spectra. Hence, bands III correspond to two almost degenerate transitions one of which is $\alpha(\sigma)$ and the other (at lower energy) π polarized.

Importantly, the energy differences between band II and its low-energy satellite IIa present in the σ spectra (Figure 6b) and between bands IIIb and IIIa in the α spectrum (Figures 6a and 7) are almost equal, viz. 2500 and 2400 cm^{-1}, respectively. Therefore, in both cases we are observing members of a progression in a high-frequency mode which can only be the asymmetric azide stretch with a frequency of 2100 cm^{-1} in the electronic ground state.[27,28] More complete evidence for the presence of such a progression is provided by the **E** || c spectrum

(27) Pate, J. E.; Ross, P. K.; Thamann, Th. J.; Reed, C. A.; Karlin, K. D.; Sorrell, Th. N.; Solomon, E. I. *J. Am. Chem. Soc.* **1989**, *111*, 5198.
(28) Tuczek, F. Unpublished results.

Table 2. Energies (cm^{-1}) and Intensities (ϵ (M^{-1} cm^{-1})) of Optical Absorption Bands for $[Cu_2(tmen)_2(\mu\text{-}N_3)(\mu\text{-}OH)](ClO_4)_2$

band	chloroform	Nujol		single crystal (α)		single crystal (σ)		single crystal (π)	
	300 K	300 K	13 K	300 K	30 K	300 K	30 K	300 K	30 K
Ia }	17 000 (280)	17 000	15 500	15 000 (150)	15 000 (75)	15 000 (150)	15 000 (120)	15 000 (200)	15 000 (240)
Ib }			18 000	17 800 (340)	17 800 (270)	17 800 (250)	17 800 (220)	17 200 (240)	17 200 (240)
IIa[a]						19 600 (80)			
II	22 000 (250)	22 000		22 000 (200)		22 100 (200)		22 000 (70)	
IIIa[b]						?	25 200 (100)	?	24 800 (50)
IIIb	27 500 (1700)	27 000	27 500	?	27 600 (400)	?	?	?	?
IIIc	30 000 (2500)	30 000	30 000						
IV	37 000 (12 600)	35 000	36 000						

[a] Probably 0 → 1 transition: 0 ↔ 0 transition assumed to be at ~17 000 cm^{-1}. [b] 0 → 0 transition.

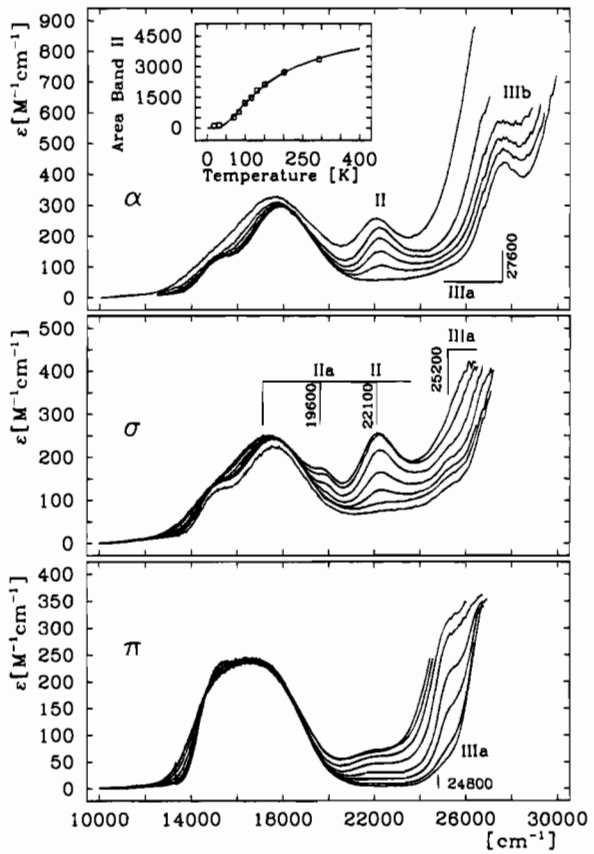

Figure 6. (a) Top: α spectra of $[Cu_2(tmen)_2(N_3)(OH)](ClO_4)_2$ at T = 293, 200, 150, 115, 82, and 32 K (top to bottom). Inset: area of band II against temperature along with fit (see text). (b) Middle: σ spectra at T = 240, 200, 150, 73, 50, and 32 K (top to bottom). (c) Bottom: π spectra at T = 250, 220, 200, 150, 100, 73, 50, and 32 K (top to bottom). Stick spectra are included to indicate progressions.

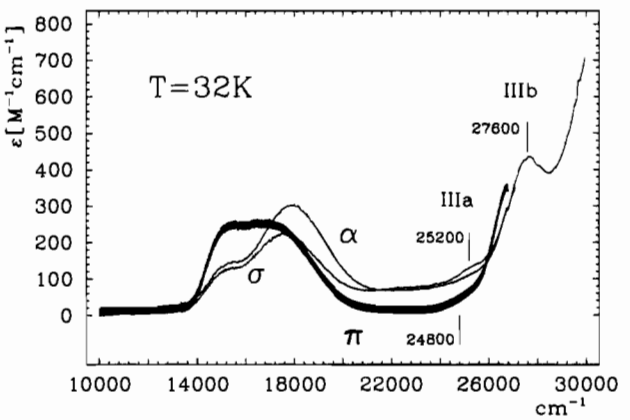

Figure 7. α, σ (solid lines) and π (bold) spectra at 32 K along with band positions.

of $[Cu_2(tbupy)_4(N_3)_2](ClO_4)_2$ (see section IIIB). In addition, band IIIc which is observed in the solution and low-temperature mull spectra (Figure 5a,b) at 30 000 cm^{-1} is again separated by 2400 cm^{-1} from band IIIb and is therefore the third member of the progression started by bands IIIa and IIIb. That band IIIa in fact corresponds to the 0 → 0 transition has been seen from the low-temperature π spectrum (*vide supra*). Thus, the splitting of band III observed in the solution and mull spectra has been found to be vibronic, not electronic, in origin, and the observation of progressions in the azide stretch associated with bands II and III allows these bands to be identified as azide → Cu CT transitions. Hence, band II and its lower energy satellite IIa correspond to an *xy* polarized azide → Cu CT transition and bands III belong to an *xy* (α,σ) and a *z* (π) polarized azide → Cu CT transition, respectively, with the *z* transition being shifted by 400 cm^{-1} toward lower energy with respect to the *xy* transition.

The temperature dependence of the single-crystal polarized absorption spectra needs further comment. Since the electronic ground state of the complex is a triplet with the singlet being $2J \geq 200$ cm^{-1} higher in energy, the intensity of singlet to singlet CT transitions should be correlated with the Boltzmann population of the singlet state, i.e. should be observable only at elevated temperatures and vanish at low temperatures. This is what is observed with band II and allows this band to be unambiguously assigned to a singlet → singlet CT transition. A plot of the area of band II vs temperature, in fact, exhibits a Boltzmann-like behavior (inset of Figure 6a). A fit of the data with the Bleaney–Bowers equation[29]

$$I \sim [1 + 3\exp(2J/kT)]^{-1} \quad (1)$$

results in a $2J$ value of 100 cm^{-1}, which is only half of the lower limit of $2J$ given in the literature. A reason for this discrepancy may be the presence of other interactions giving intensity to band II with increasing temperature besides population of the single state which lowers the effective gap between singlet and triplet states. Whereas band II has been identified as a singlet → singlet azide → Cu CT transition, bands III must correspond to triplet → triplet azide → Cu CT transitions, as their intensity does *not* vanish at low temperatures. With the spin multiplicities of bands II and III established, a final problem consists of locating the possible vibronic origin of the singlet → singlet CT transition. Since the triplet → triplet CT transition associated with bands III reaches its maximum intensity in the second to third progression, band II should also be the second or third member of the singlet → singlet CT band progression. As band IIa of the σ spectrum has at room temperature intensity comparable to that of the triplet → triplet 0 → 0 transition band IIIa at 32 K (Figure 6b), band IIa cannot be the singlet 0 → 0 transition. Consequently, band II cannot be the second but must be the third member of the progression corresponding to the 0

(29) Bleaney, B.; Bowers, K. D. *Proc. R. Soc. London* **1952**, *A214*, 451.

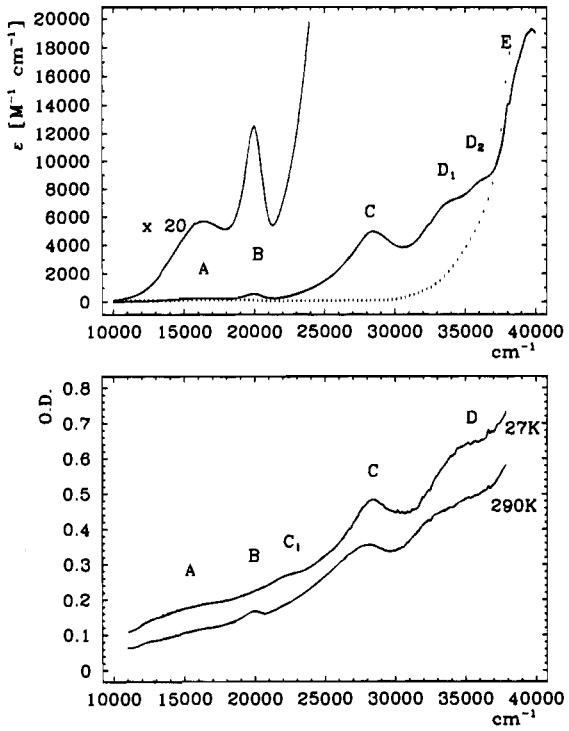

Figure 8. (a) Top: Chloroform solution spectra of $[Cu_2(tbupy)_4(N_3)_2](ClO_4)_2$ and $[Cu(tbupy)_4](ClO_4)$ (dotted). (b) Bottom: Nujol mull spectra of $[Cu_2(tbupy)_4(N_3)_2](ClO_4)_2$ at 27 and 290 K.

$\rightarrow$ 2 transition, and the singlet $\rightarrow$ singlet 0 $\rightarrow$ 0 transition has to be ~2500 cm^{-1} below band IIa.

B. tbupy. In Figure 8 the chloroform solution spectrum of $[Cu_2(tbupy)_4(N_3)_2](ClO_4)_2$ (Figure 8a, room temperature) and the Nujol mull spectra at 290 and 27 K (Figure 8b) are displayed. In the ligand field transition region, band A is observed at 16 500 cm^{-1} ($\epsilon \approx 250$ M^{-1} cm^{-1}). In the charge transfer region, four bands are observed, band B at 20 000 cm^{-1} ($\epsilon \approx 550$), band C at 28 500 cm^{-1} ($\epsilon \approx 5000$), and bands D_1 at 33 500 cm^{-1} ($\epsilon \approx$ 7000) and D_2 at 36 500 cm^{-1} ($\epsilon \approx 8600$). Finally, a high-energy, high-intensity band E is found at 39 500 cm^{-1} ($\epsilon \approx$ 19 000; see Table 3). The splitting of band D is not observed in the room-temperature Nujol spectrum; this behavior parallels that of bands IIIb and IIIc in the tmen spectra (Figure 5b). Further, it is clearly seen that band B disappears at 27 K, which corresponds to the behavior of band II in the tmen spectra. In addition, there appears a low-intensity band C_1 in the low-temperature Nujol spectrum at 22 500 cm^{-1}. For comparison, the solution spectrum of the azide-free $[Cu(tbupy)_4]^{2+}$ complex is shown in Figure 8a (dotted), indicating that bands B–D must be associated with the azide ligands, i.e. are azide $\rightarrow$ Cu CT transitions. In contrast, band E appears both in the tbupy azide dimer spectrum and in the spectrum of $[Cu(tbupy)_4]^{2+}$ and hence is probably associated with tbupy $\rightarrow$ Cu CT transitions. This also allows band IV of the tmen azide dimer spectrum (cf. section A) to be assigned to an amine $\rightarrow$ Cu CT transition. Single-crystal and solution spectra of the low-energy region of $[Cu(tbupy)_4](ClO_4)_2$ are shown in Figure 9. Bands 1 and 2 at 15 500 and 18 000 cm^{-1}, respectively, are ligand field transitions and, by comparison with the azide dimer spectra, allow the identification of band A of the tbupy azide dimer and band I of the tmen azide dimer as ligand field transitions. Note that there is no band in the region of band II showing that band II is associated with the azide ligands and is not a LF transition. In summary, there is a clear correlation between the LF azide $\rightarrow$ Cu and ligand $\rightarrow$ Cu CT transitions, respectively, between the tmen and the tbupy azide dimers which is summarized in Table 4. Importantly, band C of the tbupy spectrum has no counterpart in the tmen spectrum, and bands D_1 and D_2 are higher energy than bands IIIb and IIIc of the tmen spectrum.

In order to obtain additional information about the spectral region of the azide $\rightarrow$ Cu CT bands B and C, polarized absorption spectra in the *bc* plane of $[Cu_2(tbupy)_4(N_3)_2](ClO_4)_2$ single crystals were recorded as a function of temperature (Figure 10). Figure 10a shows the spectra for $\mathbf{E} \parallel b$ and Figure 10b for $\mathbf{E} \parallel c$. Obviously, band B disappears gradually upon cooling the sample (see inset in Figure 10b) and bands A, B, and C are much more intense for $\mathbf{E} \parallel b$ than for $\mathbf{E} \parallel c$. However, polarization assignments are now less straightforward than in the tmen system, as both spectra contain mixed molecular polarizations. Note that, for a complete determination of the ϵ tensor, three measurements are required in the case of a molecule with D_{2h} symmetry; i.e., for each wavelength, the diagonal elements of the ϵ tensor are obtained from[30]

$$\begin{bmatrix} \epsilon_a \\ \epsilon_b \\ \epsilon_c \end{bmatrix} = \mathbf{T} \begin{bmatrix} \epsilon_{xx} \\ \epsilon_{yy} \\ \epsilon_{zz} \end{bmatrix} \qquad (2)$$

where the elements of the transformation matrix **T** are given by $T_{ij} = \cos^2(x_i,a_j)$ with molecular axes x_i and directions of the **E** vector along a_j ($a_1 = a$, $a_2 = b$, $a_3 = c$). As $\mathbf{E} \parallel a$ spectra are not available (cf. section II), we take as a third data set the solution spectrum containing $^1/_3\epsilon_{xx} + {}^1/_3\epsilon_{yy} + {}^1/_3\epsilon_{zz}$. The two single-crystal spectra and the solution spectrum (all at 300 K) are plotted in Figure 11. By application of eq 2 and the transformation matrix elements of Table 5 with $\cos^2(x_i,a)$ replaced by $^1/_3$, the ϵ_{ii} values and polarizations of Table 6 are obtained. Importantly, band C is determined to be *y* polarized (i.e. along the azide vector) although the maximum of band C could not be measured in the $\mathbf{E} \parallel b$ single-crystal spectra but has been extrapolated from the slope at ~25 000 cm^{-1}. It is, however, also without this extrapolation clear that band C is not *x* polarized (along the Cu–Cu vector), as the $\mathbf{E} \parallel b$ spectrum containing 85% *x* intersects the solution spectrum containing 33% *x* at ~25 000 cm^{-1} and has a lower intensity at $\nu > 25\,000$ cm^{-1} (see Figure 11). Further, band B is found to be *x* polarized ($\parallel$ Cu–Cu), which is more detailed information as compared to that for band II in the tmen system, which was determined to be *xy* polarized ($\perp$CuCu and perpendicular to molecular plane). The temperature dependence of band B as obtained from a fit of the $\mathbf{E} \parallel c$ spectrum is plotted in Figure 10b. Fitting the data again to the Bleaney–Bowers equation (1), we determine the singlet–triplet gap to be 100 cm^{-1}, which this time agrees with the 2*J* value given in the literature. Hence, band B is shown to be a singlet $\rightarrow$ singlet azide $\rightarrow$ Cu CT transition polarized in the *x* direction (Cu–Cu vector). In contrast, band C, whose intensity shows little temperature dependence, corresponds to a triplet $\rightarrow$ triplet CT transition polarized along *y* (azide–azide vector).

Closer examination of the single-crystal spectra (Figure 10) reveals further bands at the low-energy tail of band C. Thus, band C_1 at ~22 500 cm^{-1}, which already has been observed in the low-temperature Nujol spectrum, is clearly visible in the single-crystal spectra at all temperatures. Upon cooling, a further band C_2 at 25 200 cm^{-1} can be identified. The spacing between bands C_1 and C_2, 2700 cm^{-1}, is close to the value of 2500 cm^{-1} already found in the tmen spectra (section A) and thus also corresponds to a progression in the asymmetric azide

(30) (a) Hitchman, M. A. *J. Chem. Soc., Faraday Trans. 2* **1976**, *72*, 54. (b) Hitchman, M. A. In *Transition Metal Chemistry*; Melson, G. A., Figgis, B. N., Eds.; Dekker: New York, 1985; Vol. 9, p 1.

Table 3. Energies (cm^{-1}), Intensities (ϵ (M^{-1} cm^{-1})), and Polarizations of Optical Absorption Bands for $[Cu_2(tbupy)_4(\mu\text{-}N_3)_2](ClO_4)_2$[a]

band	chloroform 300 K	Nujol 300 K	Nujol 27 K	single crystal $E \parallel b$ 300 K	single crystal $E \parallel b$ 30 K	single crystal $E \parallel c$ 300 K	single crystal $E \parallel c$ 30 K	polarization (ϵ at RT)
A_1	16 500 (250)*	16 500	16 500	16 500 (400)	15 000 (100)	16 500 (200)	14 200 (65)*	?
A_2					17 000 (200)		16 500 (120)*	x (425)
B[b]	20 000 (550)*	20 000		20 000 (1300)		20 000 (260)	20 300 (10)*	x (1410)
C_1[c]	22 500 (350)*	22 300	22 300	22 500 (700)	22 400 (300)	22 500 (100)	22 700[d] (30)*	x (770)
C_2	25 200 (1650)*	?	?	25 200 (1650)	25 200 (900)	25 200 (500)	25 200 (120)*	y (4300)
C_3				?	?	?	27 250 (415)*	
C_4	28 500 (5000)*	28 000	28 500	28 500 (3400)[e]	?	28 500 (1500)	28 550 (915)*	y (12 000)
C_5				?	?	?	30 100 (600)*	
D_1[f]	33 440 (6200)*	33 000	34 000					?
D_2	36 450 (6400)*	35 000	35 500					
E	39 640 (18 800)*							?

[a] Starred values determined by fitting. [b] Probably 0 → 2 transition; 0 → 0 transition assumed to be at ~15 000 cm^{-1} (see text). [c] 0 → 0 transition. [d] Other measurement: 22 500 cm^{-1}. [e] Approximated by extrapolation. [f] 0 → 0 transition assumed to be at ~30 000 cm^{-1} (see text).

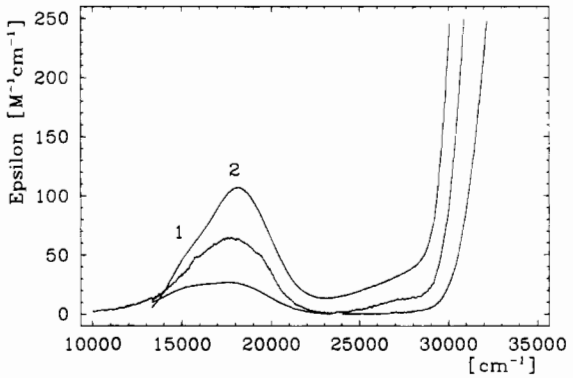

Figure 9. Spectra of $[Cu(tbupy)_4](ClO_4)_2$: (top) $\mathbf{E} \parallel b$ polarized single-crystal spectrum; (middle) $CHCl_3$ spectrum; (bottom) $\mathbf{E} \parallel c$ single-crystal spectrum; all at 300 K.

Table 4. Correlation between Bands of "tmen" (Mono μ-1,1) and "tbupy" (Bis μ-1,1)

tmen	tbupy
Ia, Ib	A_1, A_2
II	B
	C
IIIa, IIIb	D_1, D_2

stretch. The $\mathbf{E} \parallel c$ spectrum at 32 K (Figure 12) allows us to observe the full band C and to distinguish more members of this progression. Thus, a fit of this spectrum (Figure 12) locates three more members at 27 250, 28 550, and 30 100 cm^{-1} (bands C_3, C_4, and C_5). Remarkably, the spacing in this series (Table 3) first decreases in a more than anharmonic manner (2700, 2050, 1300 cm^{-1}) and then increases again (1550 cm^{-1}), and the intensity distribution (Table 3) does not follow the usual dependence

$$\frac{I_{n0}}{I_{00}} = \frac{S^n}{n!} \tag{3}$$

where I_{n0} is the intensity of the $0 \rightarrow n$ transition, S is the Huang–Rhys factor, and n corresponds to the vibrational quantum of the excited state.[31] We attribute these deviations both in spacing and in intensities from the usual characteristics to vibronic coupling with at least one higher energy CT state. In anticipation of the results of section VB, band C corresponds to the transition to the $^3B_{1g}{}^{CT}$ state which can couple with the $^3B_{3u}{}^{CT}$ state being ~7500 cm^{-1} higher energy via the antisymmetric combination of the asymmetric azide stretches of both bridging azide groups. This vibration which is of B_{2u} symmetry makes

(31) Huang, K.; Rhys, A. *Proc. R. Soc. London* **1951**, *A208*, 352.

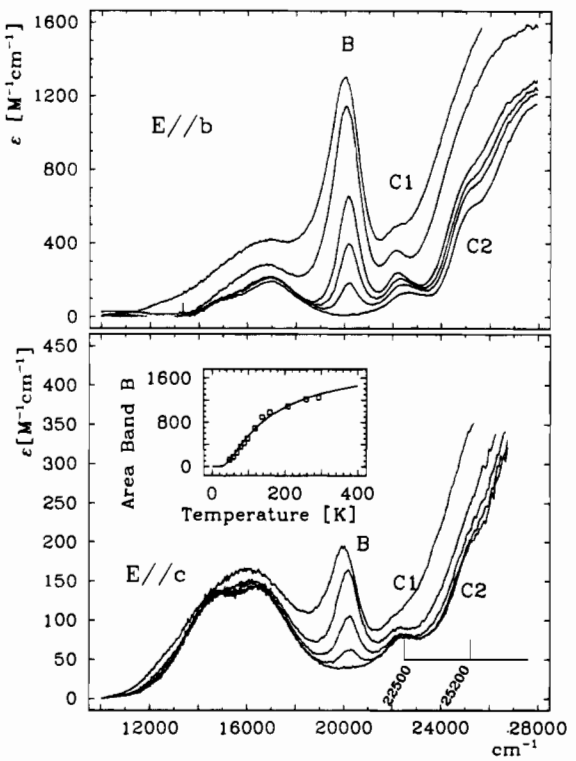

Figure 10. (a) Top: Single-crystal spectra of $[Cu_2(tbupy)_4(N_3)_2](ClO_4)_2$ for $\mathbf{E} \parallel b$ at 300, 170, 100, 80, 60, and 30 K (top to bottom). (b) Bottom: Spectrum for $\mathbf{E} \parallel c$ at 293, 160, 100, 70, and 38 K (top to bottom). Inset: area of band B vs temperature, along with fit (see text).

the vibronic coupling matrix element

$$\langle {}^3B_{1g}{}^{CT} | \partial V/\partial Q(B_{2u}) | {}^3B_{3u}{}^{CT} \rangle \neq 0 \tag{4}$$

nonvanishing and could lead to a strong deformation of CT excited state potentials, in particular in the vicinity of their crossing points. From the pattern of the spacings, the $v = 0$ level of the higher energy CT state could be at ~30 000 cm^{-1}. Assuming that band C_1 is the 0–0 transition, a Huang–Rhys factor S of about 4 can be inferred from the intensity ratio of bands C_1 and C_2 corresponding to a reorganization energy of about 10 000 cm^{-1} in the $^3B_{1g}$ CT excited state.

The atypical intensity distribution exhibited by the members of band C is found even more extremely in band B. From a comparison between the bandwidth of the individual progressions of band C and the bandwidth of band B (1000 vs 650 cm^{-1}), it follows that band B can only be one member of a progression associated with a singlet → singlet CT transition.

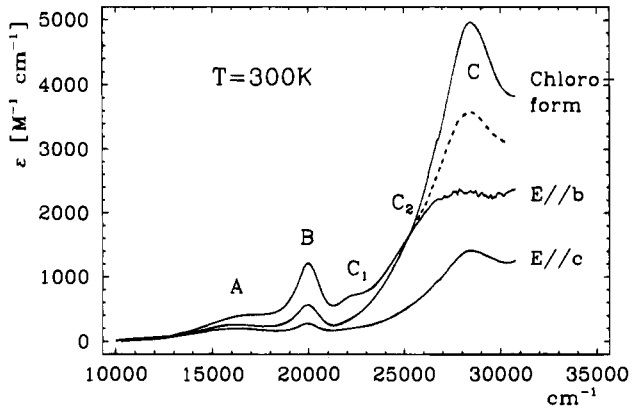

Figure 11. Single-crystal (**E** || *b*,*c*) and $CHCl_3$ solution spectra of $[Cu_2(tbupy)_4(N_3)_2](ClO_4)_2$ at room temperature. Dashed: extrapolated region of **E** || *b* spectrum.

Table 5. Transformation Matrix between Crystal and Molecular Molar Extinction Coefficients

	ϵ_{xx}	ϵ_{yy}	ϵ_{zz}
ϵ_a	3.7%	80.2%	16.1%
ϵ_b	83.5%	10.2%	6.3%
ϵ_c	10.2%	2.3%	87.5%

Table 6. Molecular Molar Extinction Coefficients and Predominant Polarization of the Electronic Transitions of $[Cu_2(tbupy)_4(N_3)_2](ClO_4)_2$ at Room Temperature

band	energy (cm^{-1})	ϵ_{xx} (M^{-1} cm^{-1})	ϵ_{yy} (M^{-1} cm^{-1})	ϵ_{zz} (M^{-1} cm^{-1})	polarizn
A	16 500	425	128	173	*x*
B	20 000	1414	108	129	*x*
C_1	22 500	771	105	131	*x*
C_2	25 200	1473	4301	301	*y*
C_3	28 500	2046	12155	813	*y*

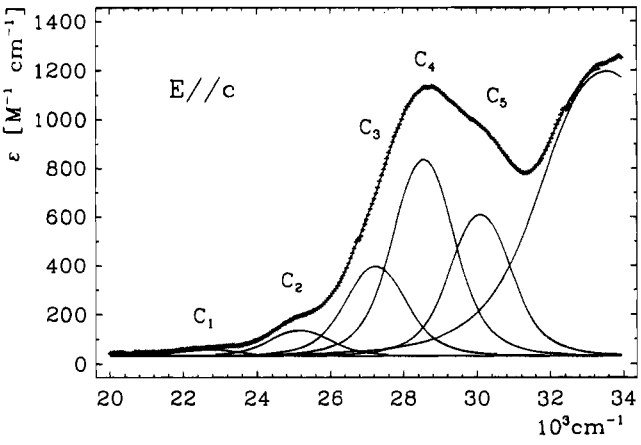

Figure 12. Band C of $[Cu_2(tbupy)_4(N_3)_2](ClO_4)_2$ at $T = 32$ K along with fit of the progression.

Note that the same applied to band II in the tmen spectrum, where, however, one further member IIa at lower energy could be observed in the σ spectrum (Figure 6b and Table 2). We assume that band **B** is the 0−2 transition and that the origin is two vibrational quanta of 2500 cm^{-1} lower in energy, i.e. at ~15 000 cm^{-1}, in analogy to band II of the tmen spectrum (section A). In this case, the band origin would be 5000 cm^{-1} lower in energy than the most intense member of the progression which approximately fits to the triplet → triplet transition associated with band C where the origin is about 6000 cm^{-1} lower in energy than the most intense member of the progression and the maximum of the room-temperature envelope, respectively.

Finally, bands D_1 and D_2 need to be considered (Figure 8a,b).

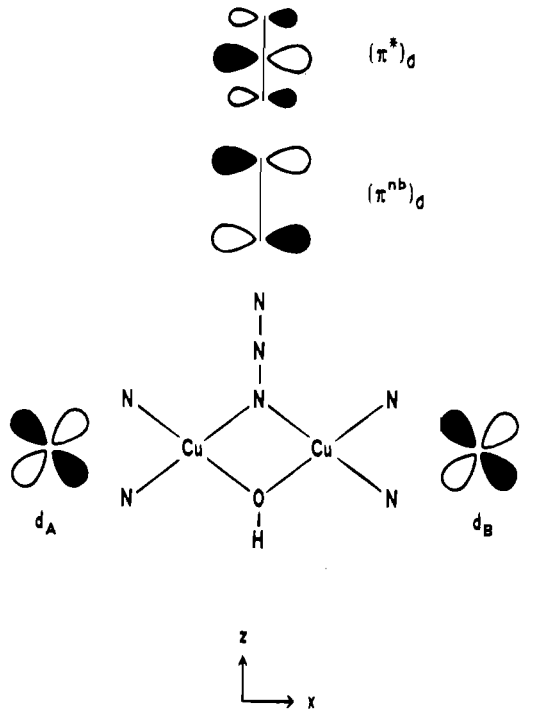

Figure 13. Mono(μ-1,1-azide) Cu(II) dimer along with coordinate system and highest singly occupied Cu d orbitals and azide HOMO and LUMO.

Due to their high intensity and their position at the slope of the high-intensity band E, their polarization cannot be determined by single-crystal transmission measurements. In view of their energy separation of about 2000 cm^{-1}, they could again be two members of a progression associated with one CT transition or two almost degenerate CT transitions as observed for bands III of the tmen system. Again, we assume that the origin of this progression is at 5000 cm^{-1} lower energy, i.e. at ~30 000 cm^{-1}.

IV. Theory

A. tmen. First, the binuclear $[Cu_2(tmen)_2(N_3)(OH)](ClO_4)_2$ complex with one μ-1,1-azide bridge and a second OH bridge (which is not included in the treatment) is considered (Figure 13). The symmetry of the dimer is C_{2v}, *z* is along the C_2 axis, and *x* is along the Cu−Cu vector (cf. sections IIA and IIIA). The copper centers are coordinated quadratically planar with their local *xy* planes lying in the molecular *xz* plane. Figure 13 also displays the highest energy Cu orbitals d_A and d_B which are both singly occupied in the ground state along with the highest (doubly) occupied in-plane orbital of the azide group, $(\pi^{nb})_\sigma$, and the lowest unoccupied in-plane orbital of azide, $(\pi^*)_\sigma$, respectively. One recognizes that by symmetry π^{nb} and π^* are both able to interact with the Cu d_{xy} orbitals in the same fashion. This is the set of four orbitals which is used to develop the valence bond CI (VBCI) description.

The next step is to consider all possible configurations within this four-orbital, four-electron picture (Scheme 2). In order to shorten our notation, the $(\pi^{nb})_\sigma$ orbital is denoted by π and the $(\pi^*)_\sigma$ orbital by π^*. In the ground state configuration GS, π is doubly and d_A and d_B are singly occupied. A (ligand → metal) charge transfer transition (CT) consists of shifting one electron from π to d_A (or to d_B), filling one Cu d orbital and leaving a hole on π. If this hole is filled by a transition of the unpaired electron on a Cu site, a configuration has been reached where one Cu orbital is empty and the other one is doubly occupied, which in effect corresponds to a metal-to-metal transition (MMCT). These three configurations, i.e. GS, CT, and MMCT,

Scheme 2

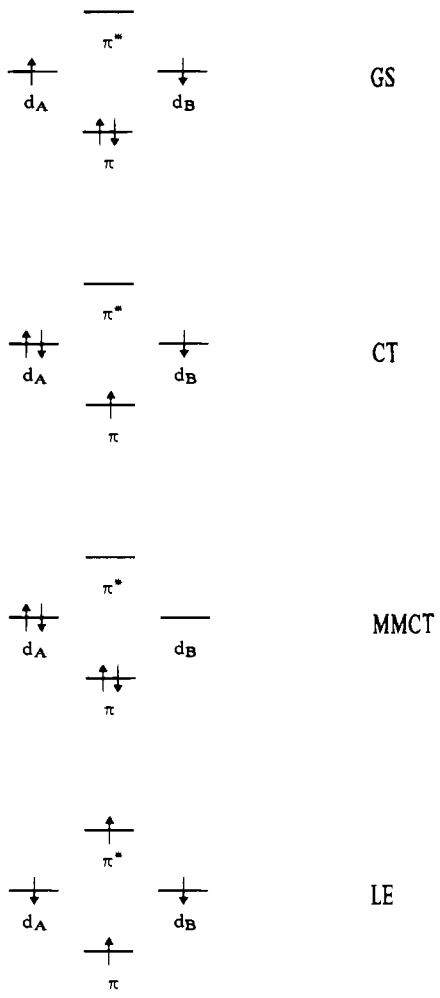

have already been described in the VBCI model for antiferromagnetically coupled dimers.[20-22] The new configuration coming into play by taking the π^* orbital into account is the ligand-excited (LE) configuration which can be reached from the CT configuration by shifting one electron from the doubly occupied Cu orbital to π^*. Thus, in the LE configuration, there are four unpaired electrons in the set of four orbitals. In principle, we would have to include two more configurations in our scheme, i.e. the double-CT (DCT) configuration with two electrons in each d orbital and π,π^* empty and a configuration with one electron in each Cu d orbital and π^* doubly occupied, which we want to leave out of the discussion because their energies are very high.

The Slater determinants corresponding to the configurations GS, CT, MMCT, and LE are compiled in Table 7. Note that the GS and CT configurations give rise to singlet and triplet configurations by coupling of the two unpaired electrons. The MMCT configuration has necessarily singlet character because all electrons are paired. By suitable linear combinations of the singlet/triplet configurations, states transforming according to the irreducible representations of the group C_{2v} can be constructed (Table 7, right). The LE states, finally, can be considered as arising from a coupling between a singlet or a triplet configuration of the metal centers and a locally excited ($\pi\pi^*$) singlet or triplet state of the ligand. Thus, a metal singlet ($S = 0$) can couple with a ligand-excited singlet ($S = 0$) to form a singlet ($S = 0$) and with a ligand-excited triplet ($S = 1$) to form a triplet ($S = 1$). A metal triplet can couple with a ligand-excited singlet to form a triplet ($S = 1$) and with a ligand-excited triplet to form a quartet, triplet, and singlet ($S = 2, 1, 0$). Hence, there are in total one quartet, two triplets, and two singlets. For future reference, we denote the LE states arising from a coupling between the metal triplet and the excited ligand triplet by a subscript t. The LE states transforming according to C_{2v} are also compiled in Table 7, right column.

Table 7. Slater Determinants and Linear Combinations for $M_S = 0$: Mono μ-1,1

Slater determinant	linear combination	state
$\lvert \bar{A}\ \bar{B}\ \bar{C}\ \bar{C}\rvert$	$= {}^{1}\Phi^{GS}$	$= -1/\sqrt{2}\,(\Phi^{GS} - \Phi^{GS})$	$= {}^{1}A_1^{GS}$
$\lvert \bar{A}\ \bar{B}\ \bar{C}\ \bar{C}\rvert$	$= {}^{2}\Phi^{GS}$	$= -1/\sqrt{2}\,(\Phi^{GS} + \Phi^{GS})$	$= {}^{3}B_1^{GS}$
$\lvert \bar{A}\ \bar{B}\ \bar{C}\ \bar{A}\rvert$	$= {}^{1}\Phi^{CT}$	$= \frac{1}{2}(\Phi^{CT} - \Phi^{CT} + \Phi^{CT} - \Phi^{CT})$	$= {}^{1}B_1^{CT}$
$\lvert \bar{A}\ \bar{B}\ \bar{C}\ \bar{A}\rvert$	$= {}^{2}\Phi^{CT}$	$= \frac{1}{2}(\Phi^{CT} - \Phi^{CT} - \Phi^{CT} + \Phi^{CT})$	$= {}^{1}A_1^{CT}$
$\lvert \bar{A}\ \bar{B}\ \bar{C}\ \bar{B}\rvert$	$= {}^{3}\Phi^{CT}$	$= \frac{1}{2}(\Phi^{CT} + \Phi^{CT} + \Phi^{CT} + \Phi^{CT})$	$= {}^{3}B_1^{CT}$
$\lvert \bar{A}\ \bar{B}\ \bar{C}\ \bar{B}\rvert$	$= {}^{4}\Phi^{CT}$	$= \frac{1}{2}(\Phi^{CT} + \Phi^{CT} - \Phi^{CT} - \Phi^{CT})$	$= {}^{3}A_1^{CT}$
$\lvert \bar{A}\ \bar{A}\ \bar{C}\ \bar{C}\rvert$	$= {}^{1}\Phi^{MMCT}$	$= 1/\sqrt{2}\,(\Phi^{MMCT} + \Phi^{MMCT})$	$= {}^{1}A_1^{MMCT}$
$\lvert \bar{B}\ \bar{B}\ \bar{C}\ \bar{C}\rvert$	$= {}^{2}\Phi^{MMCT}$	$= 1/\sqrt{2}\,(\Phi^{MMCT} - \Phi^{MMCT})$	$= {}^{1}B_1^{MMCT}$
$\lvert \bar{A}\ \bar{B}\ \bar{C}\ \bar{C}^*\rvert$	$= {}^{1}\Phi^{LE}$	$= 1/\sqrt{12}\,(2\Phi^{LE} - \Phi^{LE} - \Phi^{LE} - \Phi^{LE} - \Phi^{LE} + 2\Phi^{LE})$	$= {}^{1}{}_{t}B_1^{LE}$
$\lvert \bar{A}\ \bar{B}\ \bar{C}\ \bar{C}^*\rvert$	$= {}^{2}\Phi^{LE}$	$= \frac{1}{2}(-\Phi^{LE} + \Phi^{LE} + \Phi^{LE} - \Phi^{LE})$	$= {}^{1}A_1^{LE}$
$\lvert \bar{A}\ \bar{B}\ \bar{C}\ \bar{C}^*\rvert$	$= {}^{3}\Phi^{LE}$	$= \frac{1}{2}(\Phi^{LE} + \Phi^{LE} - \Phi^{LE} - \Phi^{LE})$	$= {}^{3}A_1^{LE}$
$\lvert \bar{A}\ \bar{B}\ \bar{C}\ \bar{C}^*\rvert$	$= {}^{4}\Phi^{LE}$	$= \frac{1}{2}(\Phi^{LE} - \Phi^{LE} + \Phi^{LE} - \Phi^{LE})$	$= {}^{3}B_1^{LE}$
$\lvert \bar{A}\ \bar{B}\ \bar{C}\ \bar{C}^*\rvert$	$= {}^{5}\Phi^{LE}$	$= 1/\sqrt{2}\,(\Phi^{LE} - \Phi^{LE})$	$= {}^{3}{}_{t}B_1^{LE}$
$\lvert \bar{A}\ \bar{B}\ \bar{C}\ \bar{C}^*\rvert$	$= {}^{6}\Phi^{LE}$	$= 1/\sqrt{6}\,(\Phi^{LE} + \Phi^{LE} + \Phi^{LE} + \Phi^{LE} + \Phi^{LE} + \Phi^{LE})$	$= {}^{5}{}_{t}B_1^{LE}$

Nomenclature:

d_{xy} orbitals of the Cu centers:	A and B	ground state:	GS
$(\pi^{nb})_\sigma$ orbital of azide ligand:	C	ligand→metal CT:	CT
$(\pi^*)_\sigma$ orbital of azide ligand:	C*	metal→metal CT:	MMCT
"spin up/down":	+/-	ligand excited state:	LE
Singlet/Triplet:	1/3		

Table 8. Off-Diagonal Matrix Elements for Mono(μ-1,1-azido) Cu(II) Dimers

GS ⟷ CT:	$\langle {}^{1}A_1^{GS} \lvert H \rvert {}^{1}A_1^{CT}\rangle = \langle {}^{3}B_1^{GS} \lvert H \rvert {}^{3}B_1^{CT}\rangle$	$= \sqrt{2}\, h_{d_A\pi}$
GS ⟷ MMCT:	$\langle {}^{1}A_1^{GS} \lvert H \rvert {}^{1}A_1^{MMCT}\rangle$	$= 0$
GS ⟷ LE:	$\langle {}^{1}A_1^{GS} \lvert H \rvert {}^{1}A_1^{LE}\rangle = \langle {}^{3}B_1^{GS} \lvert H \rvert {}^{3}B_1^{LE}\rangle$	$= 0$
	$\langle {}^{3}B_1^{GS} \lvert H \rvert {}^{3}{}_{t}B_1^{LE}\rangle$	$= 0$
CT ⟷ MMCT:	$\langle {}^{1}A_1^{CT} \lvert H \rvert {}^{1}A_1^{MMCT}\rangle = \langle {}^{1}B_1^{CT} \lvert H \rvert {}^{1}B_1^{MMCT}\rangle$	$= \sqrt{2}\, h_{d_A\pi}$
CT ⟷ LE:	$\langle {}^{1}B_1^{CT} \lvert H \rvert {}^{1}{}_{t}B_1^{LE}\rangle$	$= \sqrt{3}\, h_{d_A\pi^*}$
	$\langle {}^{1}A_1^{CT} \lvert H \rvert {}^{1}A_1^{LE}\rangle = \langle {}^{3}A_1^{CT} \lvert H \rvert {}^{3}A_1^{LE}\rangle$	$= h_{d_A\pi^*}$
	$\langle {}^{3}B_1^{CT} \lvert H \rvert {}^{3}B_1^{LE}\rangle$	$= h_{d_A\pi^*}$
	$\langle {}^{3}B_1^{CT} \lvert H \rvert {}^{3}{}_{t}B_1^{LE}\rangle$	$= \sqrt{2}\, h_{d_A\pi^*}$
MMCT ⟷ LE:	$\langle {}^{1}A_1^{MMCT} \lvert H \rvert {}^{1}A_1^{LE}\rangle = \langle {}^{1}B_1^{MMCT} \lvert H \rvert {}^{1}B_1^{LE}\rangle$	$= 0$

Having determined the relevant VB states, we now construct energy matrices for the various irreducible representations. As explained previously,[20-22] the diagonal energies of the Hamiltonian

$$H = \sum h(i) + \sum e^2/r_{ij} \qquad (5)$$

are parametrized in terms of the CT energy Δ and the energy of the MMCT state U. The energy of the LE states is denoted by $\langle\pi^*\rangle$. As before, the diagonal splittings due to the two-

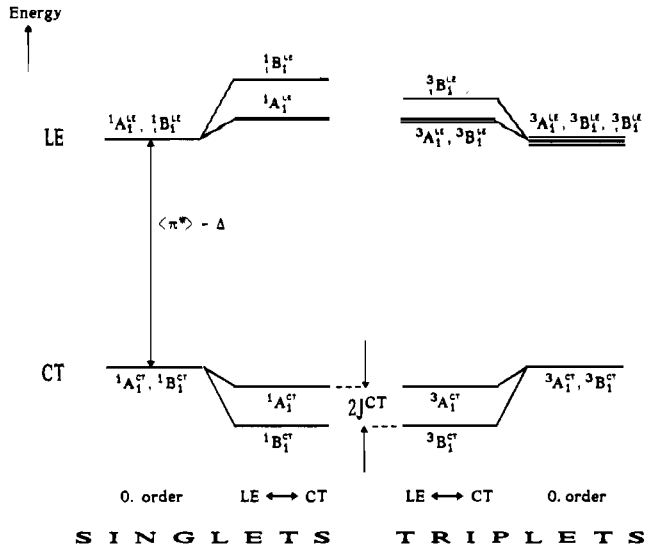

Figure 14. Charge transfer (CT)−ligand-excited (LE) state interaction for mono μ-1,1 dimers.

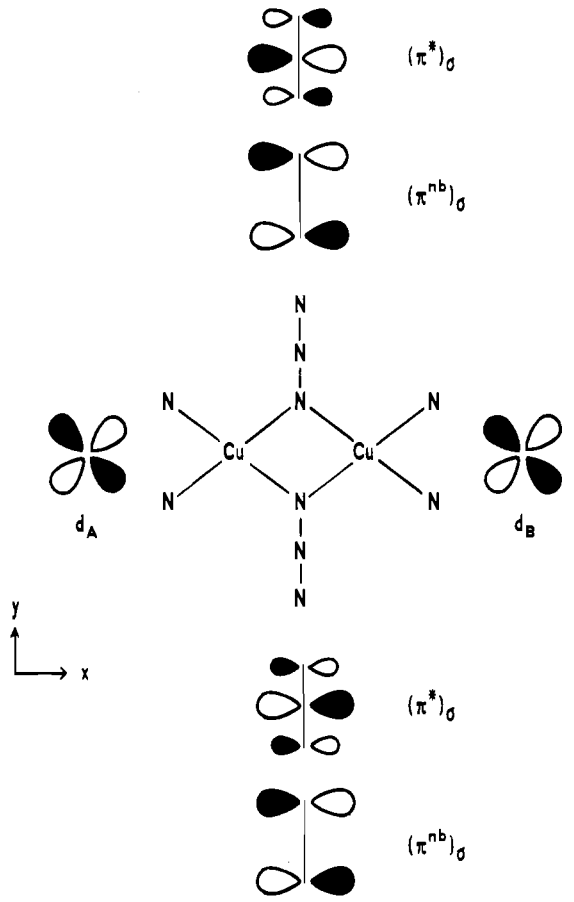

Figure 15. Bis(μ-1,1-azide) Cu(II) dimer along with coordinate system and highest singly occupied Cu d orbitals and HOMO and LUMO for the two azide groups.

electron terms in (1) are neglected. Hence, in zeroth order, all CT states are at the same energy Δ, the MMCT states are at an energy U, and all LE states are at an energy $\langle\pi^*\rangle$ above the ground state. The splitting within the GS, CT, etc. states is induced by off-diagonal elements of the one-electron part in (1) (so-called transfer matrix elements) which, in the present case, are

$$\sqrt{2}h_{d_A\pi} = \sqrt{2}\langle d_A|h|\pi\rangle \equiv h_{d\pi} \qquad (6a)$$

Scheme 3

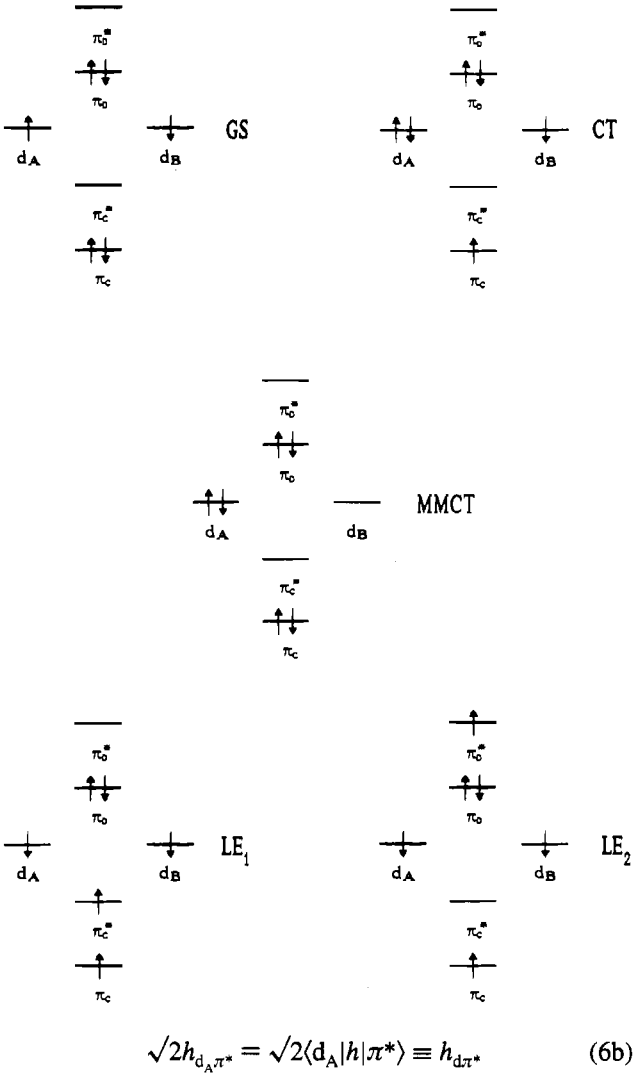

$$\sqrt{2}h_{d_A\pi^*} = \sqrt{2}\langle d_A|h|\pi^*\rangle \equiv h_{d\pi^*} \qquad (6b)$$

Table 8 gives all nonvanishing matrix elements between the states of Table 7 in terms of these off-diagonal (transfer) matrix elements. The consequences of the interactions among GS, CT, and MMCT states have been described earlier.[20-22] The new interaction CT−LE is presented in Figure 14, which displays the energy levels of the CT and LE states before (i.e. at 0 order) and after including the CT−LE off-diagonal matrix elements, respectively, in a perturbation limit ($h_{d_A\pi^*} \ll \langle\pi^*\rangle - \Delta$). Note that the CT−LE interaction acts to lower both singlet and triplet A_1^{CT} and B_1^{CT} states, but the B_1 states are 3 times stronger than the A_1^{CT} states (triplets as well as singlets). In particular, the $^3B_1^{CT}$ state is lowered with respect to the $^1A_1^{CT}$ state. This is the mechanism of ferromagnetic interaction in the CT excited state mediated by the π^* orbital (see also section VA). Further, it is seen that the major part of this selective lowering of the B_1^{CT} states is due to interaction with the $^1B_1^{LE}$ states, i.e. the B_1^{LE} states resulting from a coupling between the metal triplet and excited ligand triplet.

B. tbupy. Next, the binuclear Cu(II) azido complex $[Cu_2(tbupy)_4(N_3)_2]^{2+}$ with two μ-1,1-azide bridges (Figure 15) is considered. The symmetry of the dimer is D_{2h} with the x axis along the Cu−Cu vector, the y axis along the azide vector, and the z axis perpendicular to the molecular plane (cf. sections IIB and IIIB). Again, the coordination of the two copper centers is quadratically planar. Figure 15 also displays the highest energy Cu d orbitals d_A and d_B, which are both singly occupied in the ground state along with the highest occupied $(\pi^{nb})_\sigma$ as well as

Table 9. Slater Determinants and Linear Combinations for $M_S = 0$: Bis μ-1,1

Slater determinants

$|\overset{\uparrow}{A}\ \bar{B}\ \overset{\uparrow}{C}\ \bar{C}\ \overset{\downarrow}{D}\ \bar{D}| = {}^{1}\text{GS}$ $|\bar{A}\ \overset{\uparrow}{B}\ \overset{\downarrow}{C}\ \bar{C}\ \overset{\uparrow}{D}\ \bar{D}| = {}^{2}\text{GS}$ $|\bar{A}\ \overset{\uparrow}{B}\ \overset{\downarrow}{C}\ \bar{C}^{*}\ \overset{\uparrow}{D}\ \bar{D}| = {}^{4}\text{LE1C}$ $|\bar{A}\ \overset{\uparrow}{B}\ \overset{\downarrow}{C}\ \bar{D}^{*}\ \overset{\uparrow}{D}\ \bar{D}| = {}^{4}\text{LE2C}$

$|\overset{\uparrow}{A}\ \overset{\downarrow}{B}\ \overset{\uparrow}{C}\ \bar{A}\ \overset{\downarrow}{D}\ \bar{D}| = -{}^{1}\text{CT}$ $|\overset{\uparrow}{A}\ \overset{\downarrow}{B}\ \overset{\uparrow}{C}\ \bar{C}\ \overset{\downarrow}{D}\ \bar{A}| = {}^{3}\text{CT}$ $|\bar{A}\ \overset{\uparrow}{B}\ \overset{\downarrow}{C}\ \bar{C}^{*}\ \overset{\downarrow}{D}\ \bar{D}| = {}^{5}\text{LE1C}$ $|\bar{A}\ \overset{\uparrow}{B}\ \overset{\downarrow}{C}\ \bar{D}^{*}\ \overset{\downarrow}{D}\ \bar{D}| = {}^{5}\text{LE2C}$

$|\overset{\uparrow}{A}\ \bar{B}\ \overset{\uparrow}{C}\ \bar{A}\ \overset{\downarrow}{D}\ \bar{D}| = {}^{2}\text{CT}$ $|\overset{\uparrow}{A}\ \overset{\downarrow}{B}\ \overset{\uparrow}{C}\ \bar{C}\ \overset{\downarrow}{D}\ \bar{A}| = {}^{6}\text{CT}$ $|\bar{A}\ \overset{\uparrow}{B}\ \overset{\downarrow}{C}\ \bar{C}^{*}\ \overset{\downarrow}{D}\ \bar{D}| = {}^{6}\text{LE1C}$ $|\bar{A}\ \overset{\uparrow}{B}\ \overset{\downarrow}{C}\ \bar{D}^{*}\ \overset{\downarrow}{D}\ \bar{D}| = {}^{6}\text{LE2C}$

$|\overset{\uparrow}{A}\ \overset{\downarrow}{B}\ \bar{C}\ \bar{B}\ \overset{\uparrow}{D}\ \bar{D}| = {}^{3}\text{CT}$ $|\overset{\uparrow}{A}\ \overset{\downarrow}{B}\ \overset{\uparrow}{C}\ \bar{C}\ \bar{D}\ \bar{B}| = {}^{7}\text{CT}$ $|\overset{\uparrow}{A}\ \overset{\downarrow}{B}\ \overset{\downarrow}{C}\ \bar{C}\ \bar{D}\ \bar{D}^{*}| = -{}^{1}\text{LE1D}$ $|\overset{\uparrow}{A}\ \overset{\downarrow}{B}\ \overset{\uparrow}{C}\ \bar{C}\ \bar{D}\ \bar{C}^{*}| = {}^{1}\text{LE2D}$

$|\bar{A}\ \overset{\uparrow}{B}\ \overset{\uparrow}{C}\ \bar{B}\ \overset{\downarrow}{D}\ \bar{D}| = {}^{4}\text{CT}$ $|\bar{A}\ \overset{\uparrow}{B}\ \overset{\uparrow}{C}\ \bar{C}\ \overset{\downarrow}{D}\ \bar{B}| = {}^{8}\text{CT}$ $|\overset{\uparrow}{A}\ \bar{B}\ \overset{\downarrow}{C}\ \bar{C}\ \overset{\downarrow}{D}\ \bar{D}^{*}| = {}^{2}\text{LE1D}$ $|\overset{\uparrow}{A}\ \bar{B}\ \overset{\uparrow}{C}\ \bar{C}\ \bar{D}\ \bar{C}^{*}| = {}^{2}\text{LE2D}$

$|\bar{A}\ \overset{\uparrow}{B}\ \overset{\uparrow}{C}\ \bar{C}\ \overset{\uparrow}{D}\ \bar{B}| = {}^{1}\text{MMCT}$ $|\overset{\uparrow}{A}\ \bar{B}\ \overset{\uparrow}{C}\ \bar{C}\ \overset{\uparrow}{D}\ \bar{B}| = {}^{2}\text{MMCT}$ $|\overset{\uparrow}{A}\ \bar{B}\ \overset{\uparrow}{C}\ \bar{C}\ \bar{D}\ \overset{\downarrow}{D}^{*}| = {}^{3}\text{LE1D}$ $|\overset{\uparrow}{A}\ \bar{B}\ \overset{\uparrow}{C}\ \bar{C}\ \bar{D}\ \bar{C}^{*}| = {}^{3}\text{LE2D}$

$|\overset{\uparrow}{A}\ \overset{\downarrow}{B}\ \bar{C}\ \bar{C}^{*}\ \overset{\downarrow}{D}\ \bar{D}| = {}^{1}\text{LE1C}$ $|\overset{\uparrow}{A}\ \overset{\downarrow}{B}\ \bar{C}\ \bar{D}^{*}\ \overset{\downarrow}{D}\ \bar{D}| = {}^{1}\text{LE2C}$ $|\bar{A}\ \overset{\uparrow}{B}\ \overset{\uparrow}{C}\ \bar{C}\ \overset{\downarrow}{D}\ \overset{\downarrow}{D}^{*}| = {}^{4}\text{LE1D}$ $|\bar{A}\ \overset{\uparrow}{B}\ \overset{\uparrow}{C}\ \bar{C}\ \bar{D}\ \overset{\downarrow}{C}^{*}| = {}^{4}\text{LE2D}$

$|\overset{\uparrow}{A}\ \bar{B}\ \overset{\uparrow}{C}\ \bar{C}^{*}\ \overset{\downarrow}{D}\ \bar{D}| = -{}^{2}\text{LE1C}$ $|\overset{\uparrow}{A}\ \bar{B}\ \overset{\uparrow}{C}\ \bar{D}^{*}\ \overset{\downarrow}{D}\ \bar{D}| = -{}^{2}\text{LE2C}$ $|\bar{A}\ \overset{\uparrow}{B}\ \overset{\uparrow}{C}\ \bar{C}\ \overset{\downarrow}{D}\ \overset{\downarrow}{D}^{*}| = {}^{5}\text{LE1D}$ $|\bar{A}\ \overset{\uparrow}{B}\ \overset{\uparrow}{C}\ \bar{C}\ \bar{D}\ \overset{\downarrow}{C}^{*}| = {}^{5}\text{LE2D}$

$|\overset{\uparrow}{A}\ \bar{B}\ \overset{\uparrow}{C}\ \bar{C}^{*}\ \overset{\downarrow}{D}\ \bar{D}| = {}^{3}\text{LE1C}$ $|\overset{\uparrow}{A}\ \bar{B}\ \overset{\uparrow}{C}\ \bar{D}^{*}\ \overset{\downarrow}{D}\ \bar{D}| = -{}^{3}\text{LE2C}$ $|\bar{A}\ \overset{\uparrow}{B}\ \overset{\uparrow}{C}\ \bar{C}\ \overset{\downarrow}{D}\ \overset{\downarrow}{D}^{*}| = {}^{6}\text{LE1D}$ $|\bar{A}\ \overset{\uparrow}{B}\ \overset{\uparrow}{C}\ \bar{C}\ \bar{D}\ \overset{\downarrow}{C}^{*}| = {}^{6}\text{LE2D}$

Linear combinations and States

$1/\sqrt{2}\ [\ {}^{1}\text{GS} - {}^{2}\text{GS}\ ] = {}^{1}A_g^{GS}$

$1/\sqrt{2}\ [\ {}^{1}\text{GS} + {}^{2}\text{GS}\ ] = {}^{3}B_{3u}^{GS}$

$1/\sqrt{8}\ [\ {}^{1}\text{CT} - {}^{2}\text{CT} + {}^{3}\text{CT} - {}^{4}\text{CT} + {}^{5}\text{CT} - {}^{6}\text{CT} + {}^{7}\text{CT} - {}^{8}\text{CT}\ ] = {}^{1}B_{3u}^{CT}$

$1/\sqrt{8}\ [\ {}^{1}\text{CT} - {}^{2}\text{CT} + {}^{3}\text{CT} - {}^{4}\text{CT} - {}^{5}\text{CT} + {}^{6}\text{CT} - {}^{7}\text{CT} + {}^{8}\text{CT}\ ] = {}^{1}B_{1g}^{CT}$

$1/\sqrt{8}\ [\ {}^{1}\text{CT} - {}^{2}\text{CT} - {}^{3}\text{CT} + {}^{4}\text{CT} + {}^{5}\text{CT} - {}^{6}\text{CT} - {}^{7}\text{CT} + {}^{8}\text{CT}\ ] = {}^{1}A_g^{CT}$

$1/\sqrt{8}\ [\ {}^{1}\text{CT} - {}^{2}\text{CT} - {}^{3}\text{CT} + {}^{4}\text{CT} - {}^{5}\text{CT} + {}^{6}\text{CT} + {}^{7}\text{CT} - {}^{8}\text{CT}\ ] = {}^{1}B_{2u}^{CT}$

$1/\sqrt{8}\ [\ {}^{1}\text{CT} + {}^{2}\text{CT} + {}^{3}\text{CT} + {}^{4}\text{CT} + {}^{5}\text{CT} + {}^{6}\text{CT} + {}^{7}\text{CT} + {}^{8}\text{CT}\ ] = {}^{3}B_{3u}^{CT}$

$1/\sqrt{8}\ [\ {}^{1}\text{CT} + {}^{2}\text{CT} + {}^{3}\text{CT} + {}^{4}\text{CT} - {}^{5}\text{CT} - {}^{6}\text{CT} - {}^{7}\text{CT} - {}^{8}\text{CT}\ ] = {}^{3}B_{1g}^{CT}$

$1/\sqrt{8}\ [\ {}^{1}\text{CT} + {}^{2}\text{CT} - {}^{3}\text{CT} - {}^{4}\text{CT} + {}^{5}\text{CT} + {}^{6}\text{CT} - {}^{7}\text{CT} - {}^{8}\text{CT}\ ] = {}^{3}A_g^{CT}$

$1/\sqrt{8}\ [\ {}^{1}\text{CT} + {}^{2}\text{CT} - {}^{3}\text{CT} - {}^{4}\text{CT} - {}^{5}\text{CT} - {}^{6}\text{CT} + {}^{7}\text{CT} + {}^{8}\text{CT}\ ] = {}^{3}B_{2u}^{CT}$

$1/\sqrt{2}\ [\ {}^{1}\text{MMCT} + {}^{2}\text{MMCT}\ ] = {}^{1}A_g^{MMCT}$

$1/\sqrt{2}\ [\ {}^{1}\text{MMCT} - {}^{2}\text{MMCT}\ ] = {}^{1}B_{3u}^{MMCT}$

$1/\sqrt{24}\ [\ 2\,{}^{1}\text{LE1C} - {}^{2}\text{LE1C} - {}^{3}\text{LE1C} - {}^{4}\text{LE1C} - {}^{5}\text{LE1C} + 2\,{}^{6}\text{LE1C}$
$+ 2\,{}^{1}\text{LE1D} - {}^{2}\text{LE1D} - {}^{3}\text{LE1D} - {}^{4}\text{LE1D} - {}^{5}\text{LE1D} + 2\,{}^{6}\text{LE1D}\ ] = {}^{1}_{t}B_{3u}^{Lt}$

$1/\sqrt{24}\ [\ 2\,{}^{1}\text{LE1C} - {}^{2}\text{LE1C} - {}^{3}\text{LE1C} - {}^{4}\text{LE1C} - {}^{5}\text{LE1C} + 2\,{}^{6}\text{LE1C}$
$- 2\,{}^{1}\text{LE1D} + {}^{2}\text{LE1D} + {}^{3}\text{LE1D} + {}^{4}\text{LE1D} + {}^{5}\text{LE1D} - 2\,{}^{6}\text{LE1D}\ ] = {}^{1}_{t}B_{1g}^{Lt}$

$1/\sqrt{8}\ [\ -{}^{2}\text{LE1C} + {}^{3}\text{LE1C} + {}^{4}\text{LE1C} - {}^{5}\text{LE1C}$
$- {}^{2}\text{LE1D} + {}^{3}\text{LE1D} + {}^{4}\text{LE1D} - {}^{5}\text{LE1D}\ ] = {}^{1}A_g^{Lt}$

$1/\sqrt{8}\ [\ -{}^{2}\text{LE1C} + {}^{3}\text{LE1C} + {}^{4}\text{LE1C} - {}^{5}\text{LE1C}$
$+ {}^{2}\text{LE1D} - {}^{3}\text{LE1D} - {}^{4}\text{LE1D} + {}^{5}\text{LE1D}\ ] = {}^{1}B_{2u}^{Lt}$

$1/\sqrt{8}\ [\ {}^{2}\text{LE1C} + {}^{3}\text{LE1C} - {}^{4}\text{LE1C} - {}^{5}\text{LE1C}$
$+ {}^{2}\text{LE1D} + {}^{3}\text{LE1D} - {}^{4}\text{LE1D} - {}^{5}\text{LE1D}\ ] = {}^{3}A_g^{Lt}$

$1/\sqrt{8}\ [\ {}^{2}\text{LE1C} + {}^{3}\text{LE1C} - {}^{4}\text{LE1C} - {}^{5}\text{LE1C}$
$- {}^{2}\text{LE1D} - {}^{3}\text{LE1D} + {}^{4}\text{LE1D} + {}^{5}\text{LE1D}\ ] = {}^{3}B_{2u}^{Lt}$

$1/\sqrt{8}\ [\ {}^{2}\text{LE1C} - {}^{3}\text{LE1C} + {}^{4}\text{LE1C} - {}^{5}\text{LE1C}$
$+ {}^{2}\text{LE1D} - {}^{3}\text{LE1D} + {}^{4}\text{LE1D} - {}^{5}\text{LE1D}\ ] = {}^{3}B_{3u}^{Lt}$

$1/\sqrt{8}\ [\ {}^{2}\text{LE1C} - {}^{3}\text{LE1C} + {}^{4}\text{LE1C} - {}^{5}\text{LE1C}$
$- {}^{2}\text{LE1D} + {}^{3}\text{LE1D} - {}^{4}\text{LE1D} + {}^{5}\text{LE1D}\ ] = {}^{3}B_{1g}^{Lt}$

$1/2\ [\ {}^{1}\text{LE1C} - {}^{6}\text{LE1C} + {}^{1}\text{LE1D} - {}^{6}\text{LE1D}\ ] = {}^{3}_{t}B_{3u}^{Lt}$

$1/2\ [\ {}^{1}\text{LE1C} - {}^{6}\text{LE1C} - {}^{1}\text{LE1D} + {}^{6}\text{LE1D}\ ] = {}^{3}_{t}B_{1g}^{Lt}$

$1/\sqrt{12}\ [\ {}^{1}\text{LE1C} + {}^{2}\text{LE1C} + {}^{3}\text{LE1C} + {}^{4}\text{LE1C} + {}^{5}\text{LE1C} + {}^{6}\text{LE1C}$
$+ {}^{1}\text{LE1D} + {}^{2}\text{LE1D} + {}^{3}\text{LE1D} + {}^{4}\text{LE1D} + {}^{5}\text{LE1D} + {}^{6}\text{LE1D}\ ] = {}^{5}_{t}B_{3u}^{Lt}$

$1/\sqrt{12}\ [\ {}^{1}\text{LE1C} + {}^{2}\text{LE1C} + {}^{3}\text{LE1C} + {}^{4}\text{LE1C} + {}^{5}\text{LE1C} + {}^{6}\text{LE1C}$
$- {}^{1}\text{LE1D} - {}^{2}\text{LE1D} - {}^{3}\text{LE1D} - {}^{4}\text{LE1D} - {}^{5}\text{LE1D} - {}^{6}\text{LE1D}\ ] = {}^{5}_{t}B_{1g}^{Lt}$

Nomenclature: as in Table 7. $(\pi^{nb})_\sigma$ orbital of the second azide ligand: D; $(\pi^*)_\sigma$ orbital of the second ligand: D*

Note: the linear combinations for the LE_2 states (another 12) are formed in analogy to those of the LE_1 states (see text)

lowest unoccupied $(\pi^*)_\sigma$ orbitals of both azide groups. For convenience, the azide orbitals are denoted by π_C, π_D, π^*_C, and π^*_D with obvious meanings. Then, configurations resulting from the various possibilities to distribute six electrons (one from each copper, two from each azide) on this set of six orbitals are considered (Scheme 3). In analogy to the mono(azide)-bridged dimer, there are GS, CT, and MMCT configurations. However, there are now two different kinds of LE configurations, i.e. LE_1 with both unpaired electrons on one azide and LE_2 with the unpaired electrons on different azides. The Slater determinants corresponding to the GS, CT, MMCT, and $LE_{1,2}$ configurations are compiled in Table 9. Note that there are again one singlet and one triplet ground state, ${}^{1}A_g^{GS}$ and ${}^{3}B_{3u}^{GS}$ but that the number of CT excited states has doubled; i.e., there are now four singlet and four triplet states. The same applies to the LE states; i.e., there are now four singlets, six triplets, and two quintets for each of the LE_1 and LE_2 states. In order to construct the energy matrices, the energies and off-diagonal elements need to be evaluated and parametrized, respectively. As before, Δ and U denote the CT and MMCT zeroth-order energies. Both LE_1 and LE_2 states are supposed to be at the energy $\langle\pi^*\rangle$. The off-diagonal elements in terms of the transfer matrix elements $h_{d_A\pi}$ and $h_{d_A\pi^*}$ are compiled in Table 10. Note that both the GS−CT and CT−MMCT matrix elements are multiplied by a factor of $\sqrt{2}$ with respect to the mono(azide) dimer whereas the CT−$LE_{1,2}$ matrix elements have the same values as before. However, as the off-diagonal matrix elements enter the interaction energies squared and the LE states occur twice (*vide supra*), all interaction energies in the bis μ-1,1 dimer are effectively doubled with respect to the mono μ-1,1 dimer.

The CT−LE interaction is displayed schematically in Figure 16 in a perturbation limit ($h_{d_A\pi^*} \ll \langle\pi^*\rangle - \Delta$). Again, all CT states are lowered in energy by this interaction, but the ${}^{1,3}B_{3u}^{CT}$ and ${}^{1,3}B_{1g}^{CT}$ states are 3 times stronger than the ${}^{1,3}A_g^{CT}$ and ${}^{1,3}B_{2u}^{CT}$ states. In particular, ${}^{3}B_{3u}^{CT}$ is shifted below ${}^{1}A_g^{CT}$. This is the ferromagnetic interaction in the CT excited state via the π^* orbital. It is seen that the major part of this selective interaction with B_{1g} and B_{3u} is due to the ${}_tB_{1g}$ and ${}_tB_{3u}$ singlet and triplet $LE_{1,2}$ states, i.e. those LE states which result from coupling of the metal triplet and the ligand triplet (*vide supra*).

V. Spectral Assignments and Interpretation

A. tmen. Table 11 gives the polarizations of the allowed electronic transitions from the ${}^{3}B_1^{GS}$ triplet and ${}^{1}A_1^{GS}$ singlet ground state, respectively, to the four ${}^{1,3}\Gamma^{CT}$ azide → Cu LMCT states ($\Gamma = A_1, B_1$). On the basis of a comparison with Table 2, the singlet → singlet CT band is assigned to the ${}^{1}A_1^{GS}$ →

$^1B_1^{CT}$ transition (17 000 cm^{-1}, x polarized) and the triplet → triplet CT bands evidenced for xy as well as z polarization are assigned to $^3B_1^{GS} \rightarrow {}^3A_1^{CT}$ (25 200 cm^{-1}, x) and $^3B_1^{GS} \rightarrow {}^3B_1^{CT}$ (24 800 cm^{-1}, z), respectively (Table 11). Experimentally, there is no indication of the $^1A_1^{GS} \rightarrow {}^1A_1^{CT}$ transition; i.e., this transition must be hidden under the much more intense triplet → triplet CT transitions and thus cannot appear at lower energy than band III. Hence, the singlet CT state splitting must be large (≥8000 cm^{-1}). In contrast, the two triplet CT states both lying ~8000 cm^{-1} higher in energy than the $^1B_1^{CT}$ state are close to degenerate with a splitting of only 400 cm^{-1}. In this section, these experimental results are explained with the VBCI model outlined in the previous section.

Referring to Figure 17, we successively consider configuration interaction (CI) between states of the same symmetry (cf. the corresponding matrix elements in Table 8). Starting with the triplets (Figure 17, right), CI between the $^3B_1$ ground and CT states causes a splitting of the triplet CT states being degenerate in zeroth order; i.e., $^3B_1^{CT}$ is raised in energy (with a concomitant lowering of $^3B_1^{GS}$) and $^3A_1^{CT}$ having no partner with which to interact remains at its position. The second set of states potentially interacting with the triplet CT states are the LE states which interact with both $^3B_1^{CT}$ and $^3A_1^{CT}$ but with $^3B_1^{CT}$ 3 times more strongly than with $^3A_1^{CT}$ (cf. section IVA, Figure 14, and Table 8). Hence, this interaction acts to lower the $^3B_1^{CT}-{}^3A_1^{CT}$ gap again. As it is experimentally found that $^3B_1^{CT}$ is 400 cm^{-1} lower in energy than $^3A_1^{CT}$, the interaction CT−LE is by this amount stronger than the interaction CT−GS. As to the singlet states (left half of Figure 17), the interaction CT−GS splits $^1A_1^{CT}$ and $^1B_1^{CT}$ being degenerate in zeroth order; i.e., $^1A_1^{CT}$ is raised in energy (with a concomitant lowering of $^1A_1^{GS}$) and $^1B_1^{CT}$ remains at its position. Next, CI between the CT and the metal → metal CT (MMCT) states lowers both $^1A_1^{CT}$ and $^1B_1^{CT}$. Interaction between the singlet CT and the LE states, finally, again lowers $^1A_1^{CT}$ and $^1B_1^{CT}$ in energy but $^1B_1^{CT}$ 3 times as much as $^1A_1^{CT}$, analogous to the triplets (*vide supra*). Hence, $^1B_1^{CT}$ must be the lowest CT excited state, as it is subject to interaction with *both* MMCT *and* LE states.

The above considerations can also be formulated quantitatively in a perturbation limit ($h_{d\pi}$, $h_{d\pi^*} \ll \Delta$, U, $\langle\pi^*\rangle$): The energies of the four CT states are then given by

$$\langle {}^1A_1^{CT}\rangle = \Delta - \frac{(h_{d_A\pi^*})^2}{\langle\pi^*\rangle - \Delta} - 2\frac{(h_{d_A\pi})^2}{U - \Delta} + 2\frac{(h_{d_A\pi})^2}{\Delta} \quad (7a)$$

$$\langle {}^1B_1^{CT}\rangle = \Delta - 3\frac{(h_{d_A\pi^*})^2}{\langle\pi^*\rangle - \Delta} - 2\frac{(h_{d_A\pi})^2}{U - \Delta} \quad (7b)$$

$$\langle {}^3A_1^{CT}\rangle = \Delta - \frac{(h_{d_A\pi^*})^2}{\langle\pi^*\rangle - \Delta} \quad (7c)$$

$$\langle {}^3B_1^{CT}\rangle = \Delta - 3\frac{(h_{d_A\pi^*})^2}{\langle\pi^*\rangle - \Delta} + 2\frac{(h_{d_A\pi})^2}{\Delta} \quad (7d)$$

and the energies of the two ground states by

$$\langle {}^1A_1^{GS}\rangle = -2\frac{(h_{d_A\pi})^2}{\Delta} - 4\frac{(h_{d_A\pi})^4}{U\Delta^2} - 2\frac{(h_{d_A\pi})^2(h_{d_A\pi^*})^2}{\langle\pi^*\rangle\Delta^2} \quad (8a)$$

$$\langle {}^3B_1^{GS}\rangle = -2\frac{(h_{d_A\pi})^2}{\Delta} - 6\frac{(h_{d_A\pi})^2(h_{d_A\pi^*})^2}{\langle\pi^*\rangle\Delta^2} \quad (8b)$$

where Δ is the CT energy, U the energy of the MMCT states (Mott−Hubbard U), and $\langle\pi^*\rangle$ the energy of the LE states. Taking the CT−GS energy differences and identifying these with the measured transition energies of Table 11, we obtain the following three equations:

$$\langle {}^1B_1^{CT}\rangle - \langle {}^1A_1^{GS}\rangle = \Delta' - 3\frac{(h_{d_A\pi^*})^2}{\langle\pi^*\rangle - \Delta} - 2\frac{(h_{d_A\pi})^2}{U - \Delta} + 2\frac{(h_{d_A\pi})^2}{\Delta} = 17\,000 \text{ cm}^{-1} \quad (9a)$$

$$\langle {}^3A_1^{CT}\rangle - \langle {}^3B_1^{GS}\rangle = \Delta' - \frac{(h_{d_A\pi^*})^2}{\langle\pi^*\rangle - \Delta} + 2\frac{(h_{d_A\pi})^2}{\Delta} = 25\,200 \text{ cm}^{-1} \quad (9b)$$

$$\langle {}^3B_1^{CT}\rangle - \langle {}^3B_1^{GS}\rangle = \Delta' - 3\frac{(h_{d_A\pi^*})^2}{\langle\pi^*\rangle - \Delta} + 4\frac{(h_{d_A\pi})^2}{\Delta} = 24\,800 \text{ cm}^{-1} \quad (9c)$$

with

$$\Delta' = \Delta + 4\frac{(h_{d_A\pi})^4}{U\Delta^2} + 2\frac{(h_{d_A\pi})^2(h_{d_A\pi^*})^2}{\langle\pi^*\rangle\Delta^2} \approx \Delta + 6\frac{(h_{d_A\pi})^2(h_{d_A\pi^*})^2}{\langle\pi^*\rangle\Delta^2} \quad (9d)$$

Setting $1/\Delta \approx 1/(U - \Delta)$, we can extract the following parameters by suitable linear combinations of (9a)−(9c):

$$W_{GS}^{CT} \equiv 2\frac{(h_{d_A\pi})^2}{\Delta} = 3900 \text{ cm}^{-1} \quad (10a)$$

$$W_{MMCT}^{CT} \equiv 2\frac{(h_{d_A\pi})^2}{U - \Delta} = 3900 \text{ cm}^{-1} \quad (10b)$$

$$W_{LE}^{CT} \equiv 2\frac{(h_{d_A\pi^*})^2}{\langle\pi^*\rangle - \Delta} = 4300 \text{ cm}^{-1} \quad (10c)$$

$$\Delta' = 23\,450 \text{ cm}^{-1} \quad (10d)$$

From photoelectron spectroscopy, U is known to be 6.5 eV,[32] and the energy of the azide $\langle\pi^*\rangle$ orbital has been determined to be 5.4 eV.[25] With $\Delta \approx \Delta'$, we obtain from (10a)−(10c) $\sqrt{2}h_{d_A\pi^*}$ = 9300 cm^{-1} and $\sqrt{2}h_{d_A\pi} \approx 10\,000$ cm^{-1}. We further find

$$W_{MMCT}^{GS} \equiv 4\frac{(h_{d_A\pi})^4}{U\Delta^2} = 347 \text{ cm}^{-1} \quad (11a)$$

$$W_{LE}^{GS} \equiv 4\frac{(h_{d_A\pi})^2(h_{d_A\pi^*})^2}{\langle\pi^*\rangle\Delta^2} = 350 \text{ cm}^{-1} \quad (11b)$$

and with (9d) and (10d) $\Delta \approx \Delta' - 525 = 22\,925$ cm^{-1} (see Table 12). Using (7)−(11), we calculated the energies of the GS and CT states as well as the optical transition energies in Figure 17. Whereas the $^1A_1^{GS} \rightarrow {}^1B_1^{CT}$, the $^3B_1^{CT} \rightarrow {}^3A_1^{CT}$,

(32) Didziulis, S. V.; Cohen, S. L.; Gewirth, A. A.; Solomon, E. I. *J. Am. Chem. Soc.* **1988**, *110*, 250.

Table 10. Off-Diagonal Matrix Elements for Bis(μ-1,1-azido) Cu(II) Dimers

GS ⟷ CT:	$\langle {}^1A_g^{GS} \vert H \vert {}^1A_g^{CT} \rangle$	$= \langle {}^3B_{3u}^{GS} \vert H \vert {}^3B_{3u}^{CT} \rangle$	$= 2h_{d_A\pi}$
GS ⟷ MMCT:	$\langle {}^1A_g^{GS} \vert H \vert {}^1A_g^{MMCT} \rangle$		$= 0$
GS ⟷ $LE_{1,2}$:	$\langle {}^1A_g^{GS} \vert H \vert {}^1A_g^{LE} \rangle$	$= \langle {}^3B_{3u}^{GS} \vert H \vert {}^3B_{3u}^{LE} \rangle$	$= 0$
	$\langle {}^3B_{3u}^{GS} \vert H \vert {}^3_tB_{3u}^{LE} \rangle$		$= 0$
CT ⟷ MMCT:	$\langle {}^1A_g^{CT} \vert H \vert {}^1A_g^{MMCT} \rangle$	$= \langle {}^1B_{3u}^{CT} \vert H \vert {}^1B_{3u}^{MMCT} \rangle$	$= 2h_{d_A\pi}$
CT ⟷ $LE_{1,2}$:	$\langle {}^1B_{1g}^{CT} \vert H \vert {}^1_tB_{1g}^{LE} \rangle$	$= \langle {}^1B_{3u}^{CT} \vert H \vert {}^1_tB_{3u}^{LE} \rangle$	$= \sqrt{3}\, h_{d_A\pi^*}$
	$\langle {}^1A_g^{CT} \vert H \vert {}^1A_g^{LE} \rangle$	$= \langle {}^1B_{2u}^{CT} \vert H \vert {}^1B_{2u}^{LE} \rangle$	$= h_{d_A\pi^*}$
	$\langle {}^3A_g^{CT} \vert H \vert {}^3A_g^{LE} \rangle$	$= \langle {}^3B_{1g}^{CT} \vert H \vert {}^3B_{1g}^{LE} \rangle$	$= h_{d_A\pi^*}$
	$\langle {}^3B_{2u}^{CT} \vert H \vert {}^3B_{2u}^{LE} \rangle$	$= \langle {}^3B_{3u}^{CT} \vert H \vert {}^3B_{3u}^{LE} \rangle$	$= h_{d_A\pi^*}$
	$\langle {}^3B_{1g}^{CT} \vert H \vert {}^3_tB_{1g}^{LE} \rangle$	$= \langle {}^3B_{3u}^{CT} \vert H \vert {}^3_tB_{3u}^{LE} \rangle$	$= \sqrt{2}\, h_{d_A\pi^*}$
MMCT ⟷ $LE_{1,2}$:	$\langle {}^1A_g^{MMCT} \vert H \vert {}^1A_g^{LE} \rangle$	$= \langle {}^1B_{3u}^{MMCT} \vert H \vert {}^1B_{3u}^{LE} \rangle$	$= 0$

Table 11. Polarizations of Allowed CT Transitions and Assignments for Mono μ-1,1

LMCT transition	polarizn	band	$E(0\rightarrow0)$ (cm^{-1})	ϵ_{max} ($M^{-1}\,cm^{-1}$)
${}^1A_1{}^{GS} \rightarrow {}^1A_1{}^{CT}$	z		$\geq 25\,000$	
${}^1A_1{}^{GS} \rightarrow {}^1B_1{}^{CT}$	x	II	17 000	250[a]
${}^3B_1{}^{GS} \rightarrow {}^3A_1{}^{CT}$	x	III	25 200	2500[b]
${}^3B_1{}^{GS} \rightarrow {}^3B_1{}^{CT}$	z	III	24 800	2500[b]

[a] Single crystal. [b] Solution, room temperature.

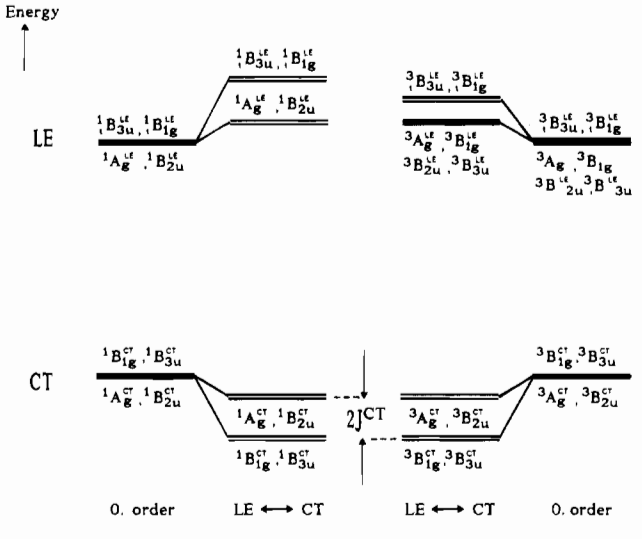

Figure 16. Charge transfer (CT)−ligand-excited (LE) state interaction for bis μ-1,1 dimers.

Table 12. VBCI Parameters for Mono μ-1,1 and Bis μ-1,1 (cm^{-1})

	mono	bis		mono	bis
Δ	22900	24800	$h_{d_A\pi^*}$	−6580	−5700
U	52400	52400	$2J^{CT}$	+400	0
$\langle\pi^*\rangle$	43500	43500	$2J^{GS}$ [a]	+26	−140
$h_{d_A\pi}$	−7070	−7020			

[a] From a diagonalization of the singlet and triplet energy matrices.

and the ${}^3B_1{}^{GS} \rightarrow {}^3B_1{}^{CT}$ transition energies, of course, must correspond to those measured experimentally, the ${}^1A_1{}^{GS} \rightarrow {}^1A_1{}^{CT}$ transition energy and the energy of the ${}^1A_1{}^{CT}$ level are *predicted* by the model. It is seen that the ${}^1A_1{}^{CT}$ level lies *above* ${}^3B_1{}^{CT}$ corresponding to a *ferromagnetic interaction in the CT excited state* (ESF, excited state ferromagnetism):

Table 13. Polarization of Allowed Transitions and Assignments for Bis μ-1,1

transition	polarizn	band	$E(0\rightarrow0)$ (cm^{-1})	ϵ_{max} ($M^{-1}\,cm^{-1}$)[a]
${}^1A_g{}^{GS} \rightarrow {}^1B_{2u}{}^{CT}$	y			
${}^1A_g{}^{GS} \rightarrow {}^1B_{3u}{}^{CT}$	x	B	15 000	550
${}^3B_{3u}{}^{GS} \rightarrow {}^3B_{1g}{}^{CT}$	y	C	22 500	5000
${}^3B_{3u}{}^{GS} \rightarrow {}^3A_g{}^{CT}$	x	D	30 000	8000

[a] Solution, room temperature.

$$2J^{CT} \equiv E({}^1A_1{}^{CT}) - E({}^3B_1{}^{CT}) = W_{LE}^{CT} - W_{MMCT}^{CT} = +400\ cm^{-1} \quad (12)$$

Obviously, W_{LE}^{CT} acts as a ferromagnetic interaction and W_{MMCT}^{CT} as an antiferromagnetic interaction in the CT excited state, and an overall ferromagnetic interaction in the CT excited state (ESF) results since W_{LE}^{CT} is larger than W_{MMCT}^{CT}. Likewise, the model predicts a very weak ferromagnetic interaction in the ground state (GSF, ground state ferromagnetism)

$$2J^{GS} \equiv E({}^1A_1{}^{GS}) - E({}^3B_1{}^{GS}) = W_{LE}^{GS} - W_{MMCT}^{GS} = +3\ cm^{-1} \quad (13)$$

and it is seen that, in analogy to the CT excited state, W_{LE}^{GS} acts as a ferromagnetic and W_{MMCT}^{GS} as an antiferromagnetic interaction in the ground state and overall ferromagnetic interaction results since W_{LE}^{GS} is slightly larger than W_{MMCT}^{GS}. A diagonalization of the energy matrices gives a value of $+26\ cm^{-1}$ for $2J^{GS}$. For a complete treatment, the above value of $2J^{GS}$ has to be augmented by the GS exchange integral.

B. tbupy. In Table 13, the selection rules for the transitions from the ${}^3B_{3u}{}^{GS}$ triplet and the ${}^1A_g{}^{GS}$ ground states to the eight ${}^{1,3}\Gamma_i{}^{CT}$, $\Gamma_i = A_g$, B_{3u}, B_{1g}, and B_{2u}, CT excited states are given. Note that there are, in analogy to the tmen system, two allowed singlet → singlet transitions along x (Cu−Cu vector) and y (azide vector) and two allowed triplet → triplet transitions along x and y (note that y in the tbupy system corresponds to z in the tmen system, cf. Figures 13 and 15). By comparison with Table 3, the singlet → singlet transition is assigned to ${}^1A_g{}^{GS} \rightarrow {}^1B_{3u}{}^{CT}$ and the triplet → triplet transition associated with band C to ${}^3B_{3u}{}^{GS} \rightarrow {}^3B_{1g}{}^{CT}$. The higher energy triplet → triplet transition associated with bands D are assigned to ${}^3B_{3u}{}^{GS} \rightarrow {}^3A_g{}^{CT}$ (x polarized). Again, there is no indication of the ${}^1A_g{}^{GS} \rightarrow {}^1A_g{}^{CT}$ transition in the spectrum. Hence, this transition must be hidden under the more intense triplet → triplet CT band and the position of band C (28 400 cm^{-1}) represents a lower limit for this transition. Table 13 summarizes these assignments.

The VBCI scheme in Figure 18 is constructed in analogy to section A. The four triplet CT excited states (Figure 18, right) are first subject to interaction with ${}^3B_{3u}{}^{GS}$ (which raises ${}^3B_{3u}{}^{CT}$ in energy) and then with the manifold of triplet LE states (Figure 18, right to center). On the basis of the interaction matrix elements given in Table 10, ${}^3B_{3u}{}^{CT}$ and ${}^3B_{1g}{}^{CT}$ are depressed in energy 3 times as much as ${}^3A_g{}^{CT}$ and ${}^3B_{2u}{}^{CT}$. As to the singlets (Figure 18, left to center), interaction between ${}^1A_g{}^{GS}$ and the manifold of singlet CT excited states raises ${}^1A_g{}^{CT}$ in energy. Due to interaction with the metal → metal CT (MMCT) states, both ${}^1A_g{}^{CT}$ and ${}^1B_{3u}{}^{CT}$ are lowered in energy, and interaction between the singlet CT and singlet LE states leads, in analogy to the triplet CT states, to a depression of ${}^1B_{3u}{}^{CT}$ and ${}^1B_{1g}{}^{CT}$ which is 3 times stronger than the depression of ${}^1A_g{}^{CT}$ and ${}^1B_{2u}{}^{CT}$.

In the perturbation limit of section A, the above considerations can be formulated quantitatively. The energies of the eight CT states are given by

$$\langle {}^1A_g{}^{CT}\rangle = \Delta - 2\frac{(h_{d_A\pi^*})^2}{\langle\pi^*\rangle - \Delta} - 4\frac{(h_{d_A\pi})^2}{U-\Delta} + 4\frac{(h_{d_A\pi})^2}{\Delta} \quad (14a)$$

$$\langle {}^1B_{1g}{}^{CT}\rangle = \Delta - 6\frac{(h_{d_A\pi^*})^2}{\langle\pi^*\rangle - \Delta} \quad (14b)$$

$$\langle {}^1B_{2u}{}^{CT}\rangle = \Delta - 2\frac{(h_{d_A\pi^*})^2}{\langle\pi^*\rangle - \Delta} \quad (14c)$$

$$\langle {}^1B_{3u}{}^{CT}\rangle = \Delta - 6\frac{(h_{d_A\pi^*})^2}{\langle\pi^*\rangle - \Delta} - 4\frac{(h_{d_A\pi})^2}{U-\Delta} \quad (14d)$$

$$\langle {}^3A_g{}^{CT}\rangle = \Delta - 2\frac{(h_{d_A\pi^*})^2}{\langle\pi^*\rangle - \Delta} \quad (14e)$$

$$\langle {}^3B_{1g}{}^{CT}\rangle = \Delta - 6\frac{(h_{d_A\pi^*})^2}{\langle\pi^*\rangle - \Delta} \quad (14f)$$

$$\langle {}^3B_{2u}{}^{CT}\rangle = \Delta - 2\frac{(h_{d_A\pi^*})^2}{\langle\pi^*\rangle - \Delta} \quad (14g)$$

$$\langle {}^3B_{3u}{}^{CT}\rangle = \Delta - 6\frac{(h_{d_A\pi^*})^2}{\langle\pi^*\rangle - \Delta} + 4\frac{(h_{d_A\pi})^2}{\Delta} \quad (14h)$$

and the energies of the ground states by

$$\langle {}^1A_g{}^{GS}\rangle = -4\frac{(h_{d_A\pi})^2}{\Delta} - 16\frac{(h_{d_A\pi})^4}{U\Delta^2} - 8\frac{(h_{d_A\pi})^2(h_{d_A\pi^*})^2}{\langle\pi^*\rangle\Delta^2} \quad (15a)$$

$$\langle {}^3B_{3u}\rangle = -4\frac{(h_{d_A\pi})^2}{\Delta} - 24\frac{(h_{d_A\pi})^2(h_{d_A\pi^*})^2}{\langle\pi^*\rangle\Delta^2} \quad (15b)$$

where the parameters have the same meaning as in section A. Taking the GS−CT energy differences and identifying these with the measured transition energies from Table 13, we obtain the following three equations with $1/\Delta \approx 1/(U-\Delta)$:

$$\langle {}^1B_{3u}{}^{CT}\rangle - \langle {}^1A_g{}^{GS}\rangle = \Delta' - 6\frac{(h_{d_A\pi^*})^2}{\langle\pi^*\rangle - \Delta} - 4\frac{(h_{d_A\pi})^2}{U-\Delta} + 4\frac{(h_{d_A\pi})^2}{\Delta} = 15\,000\ \text{cm}^{-1} \quad (16a)$$

$$\langle {}^3A_g{}^{CT}\rangle - \langle {}^3B_{3u}{}^{GS}\rangle = \Delta' - 2\frac{(h_{d_A\pi^*})^2}{\langle\pi^*\rangle - \Delta} + 4\frac{(h_{d_A\pi})^2}{\Delta} = 30\,000\ \text{cm}^{-1} \quad (16b)$$

$$\langle {}^3B_{1g}{}^{CT}\rangle - \langle {}^3B_{3u}{}^{GS}\rangle = \Delta' - 6\frac{(h_{d_A\pi^*})^2}{\langle\pi^*\rangle - \Delta} + 4\frac{(h_{d_A\pi})^2}{\Delta} = 22\,500\ \text{cm}^{-1} \quad (16c)$$

where

$$\Delta' = \Delta + 16\frac{(h_{d_A\pi})^4}{U\Delta^2} + 8\frac{(h_{d_A\pi})^2(h_{d_A\pi^*})^2}{\langle\pi^*\rangle\Delta^2} \approx \Delta + 24\frac{(h_{d_A\pi})^2(h_{d_A\pi^*})^2}{\langle\pi^*\rangle\Delta^2} \quad (16d)$$

By suitable linear combinations of (16a)−(16c), we obtain

$$W_{GS}^{CT} \equiv 4\frac{(h_{d_A\pi})^2}{\Delta} = 7500\ \text{cm}^{-1} \quad (17a)$$

$$W_{MMCT}^{CT} \equiv 4\frac{(h_{d_A\pi})^2}{U-\Delta} = 7500\ \text{cm}^{-1} \quad (17b)$$

$$W_{LE}^{CT} \equiv 4\frac{(h_{d_A\pi^*})^2}{\langle\pi^*\rangle - \Delta} = 7500\ \text{cm}^{-1} \quad (17c)$$

$$\Delta' = 26\,250\ \text{cm}^{-1} \quad (17d)$$

With the values for U and $\langle\pi^*\rangle$ given in section A, we further obtain with $\Delta \approx \Delta'$, $2h_{d_A\pi} = -14\,030\ \text{cm}^{-1}$ and $2h_{d_A\pi^*} = -11\,390\ \text{cm}^{-1}$ (cf. Table 12)

$$W_{MMCT}^{GS} \equiv 16\frac{(h_{d_A\pi})^4}{U\Delta^2} = 1070\ \text{cm}^{-1} \quad (18a)$$

$$W_{LE}^{GS} \equiv 16\frac{(h_{d_A\pi})^2(h_{d_A\pi^*})^2}{\langle\pi^*\rangle\Delta^2} = 850\ \text{cm}^{-1} \quad (18b)$$

and from (16d) and (17d) $\Delta \approx \Delta' - 1.5 \times 950\ \text{cm}^{-1} = 24\,825\ \text{cm}^{-1}$. Using (14)−(18), we calculated the GS and CT energies as well as the optical transition energies in Figure 18. Note that ${}^1B_{3u}{}^{CT}$ becomes the lowest CT excited state, as it is subject to interaction both with the MMCT and with the LE states. The ${}^3B_{1g}{}^{CT}$ level associated with band C has no counterpart in the tmen spectra, since it is subject to the full LE interaction but (unlike ${}^3B_1{}^{CT}$) has no interaction with the ground state. On the other hand, since ${}^3B_{1g}{}^{CT}$ has no interaction with the MMCT states, the energy difference between ${}^3B_{1g}{}^{CT}$ and ${}^1B_{1g}{}^{CT}$ directly provides an experimental measure of the MMCT−CT energy W_{MMCT}^{CT} responsible for the antiferromagnetic interaction in the CT excited state. Further, the ${}^1A_g$ state is at exactly the same energy as the ${}^3B_{3u}$ CT state since

$$2J^{CT} \equiv E({}^3B_{3u}{}^{CT}) - E({}^1A_g{}^{CT}) = W_{LE}^{CT} - W_{MMCT}^{CT} = 0 \quad (19)$$

Therefore, there is only a *compensation* of the ferro- and antiferromagnetic contributions in the CT excited state of the tbupy system, in contrast to the tmen system, where net ferromagnetic coupling was found with $2J^{CT} = 400\ \text{cm}^{-1}$ (section A). In the ground state, even a net antiferromagnetic interaction is found:

$$2J^{GS} \equiv E({}^3B_{3u}{}^{GS}) - E({}^1A_g{}^{GS}) = W_{LE}^{GS} - W_{MMCT}^{GS} = -220\ \text{cm}^{-1} \quad (20)$$

The value found from a diagonalization of the energy matrices is somewhat smaller, i.e. $-140\ \text{cm}^{-1}$, which is $-180\ \text{cm}^{-1}$ lower than the value for tmen. Note that, from the experimental data, $-2J$ of tbupy should be at least $-100\ \text{cm}^{-1}$ lower than $-2J$ of tmen. Of course, the GS exchange integral has to be added

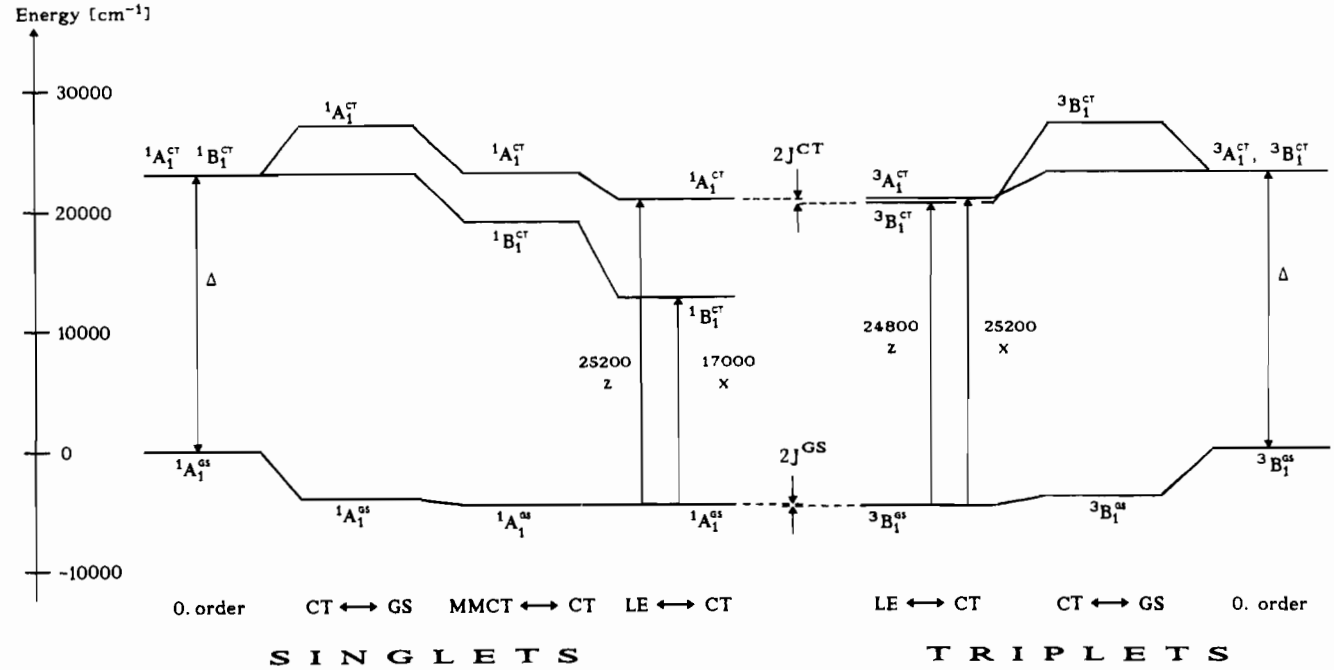

Figure 17. VBCI scheme for mono(μ-1,1-azide)-bridged dimers: right to middle, triplets; left to middle, singlets (see text).

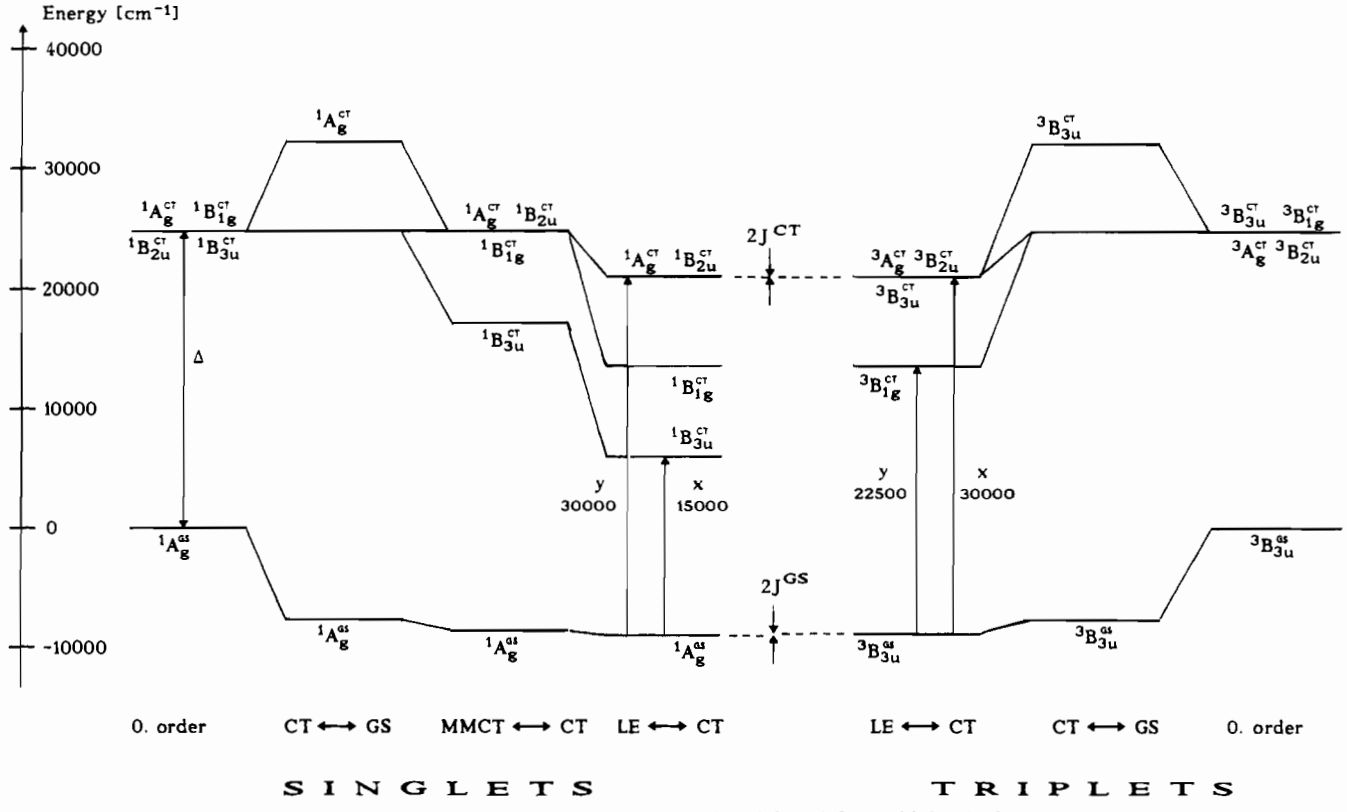

Figure 18. VBCI scheme for bis(μ-1,1-azide)-bridged dimer: right to middle, triplets; left to middle, singlets.

again and should have a value of +240 cm^{-1} in order to reach the measured $2J$ value of 100 cm^{-1}. The lower limit of the exchange integral derived from the parallel treatment of the tmen system was +170 cm^{-1}.

In summary, the CT excited state structure of the tbupy system can also be parametrized with the VBCI model. In contrast to the tmen system, there is no net magnetic coupling in the CT excited state, meaning that the antiferromagnetic and ferromagnetic interactions exactly cancel and the predicted GS coupling constant (without exchange integral) is negative. The VBCI parameters and magnetic coupling constants are compiled in Table 12. In addition, the VBCI description is also able to explain in detail the correlation between the azide → Cu CT spectra of both dimers (Table 4) covering ranges of 17 000–30 000 in the tmen and even 15 000–36 000 cm^{-1} in the tbupy system, respectively. Thus, the transfer matrix elements are of equal order of magnitude for tbupy and tmen, but for tbupy all interaction energies W are multiplied by a factor of 2 with respect to tmen. Hence, bands D are shifted to the UV with respect to the corresponding bands III of tmen. On the other hand, there appears a "new" band (C) in the tbupy system at the position of bands III, and the energy of the lowest singlet → singlet CT transition is even shifted to lower energy in the tbupy as compared to the tmen system.

VI. Discussion

The preceding section has shown that the CT excited level structure of both mono(μ-1,1-azide)- and bis(μ-1,1-azide)-bridged dimers can be parametrized in terms of the VBCI model, including the highest occupied $(\pi^{nb})_\sigma$ and the lowest unoccupied $(\pi^*)_\sigma$ orbitals of azide and the highest, singly occupied d orbitals of the two copper centers. In the azide → Cu CT states, ferro- and antiferromagnetic interactions directly compete and therefore also are directly accessible by optical absorption spectroscopy whereas, in the ground state, these interactions are only transmitted indirectly and, hence, are much smaller. In addition, the experimental information from the CT states is much greater due to the greater number of states as compared to the two singlet and triplet ground states with only one energy difference, $2J^{GS}$. Thus, the splitting of the triplet → triplet CT transitions provides a measure of the HOMO−LUMO splitting, which is found to be small, in accordance with MO theoretical concepts of exchange (see below). The strong energetic lowering of the first CT bands the singlet → singlet CT transitions II and B, respectively, can be explained in the framework of the model by a simultaneous interaction of the $^1B_1{}^{CT}$ and $^1B_{1g}{}^{CT}$ states, respectively, with the corresponding MMCT and LE states. By comparison with the transition energies of triplet → triplet CT transitions, the two interaction energies can further be separated, allowing us to obtain estimates of the antiferro- (MMCT) and ferromagnetic (LE) contributions to the excited state coupling constant $2J^{CT}$. Since both contributions are found to be of almost equal magnitude, the resulting value of $2J^{CT}$ is relatively small, i.e. 400 cm^{-1} for tmen and 0 cm^{-1} for tbupy. The calculated ground state coupling constants are $2J^{GS} = +26$ cm^{-1} for tmen and -140 cm^{-1} for tbupy. In view of the difficulty to unambiguously locate the origin of the singlet → singlet CT transition B (which directly influences this result), we do not want to overinterpret this difference. Qualitatively, there is also in the case of the tbupy system a compensation of antiferro- and ferromagnetic contributions, with the ferromagnetic contribution being weaker than in the tmen system, in agreement with the experimental findings. Of course, the ground state exchange integral (whose value is not known) has to be added to our $2J^{GS}$ value for a comparison with the experimentally determined $2J$ values.

In order to account for the ferromagnetic interaction, the π^* orbital of the azide group was included into the VBCI treatment with all possible excited configurations. This way, we found that the transfer matrix elements between the occupied $(\pi^{nb})_\sigma$ orbital, $h_{d\pi}$, and the first unoccupied $(\pi^*)_\sigma$ orbital are of equal magnitude (~7000 cm^{-1}) and the π^* orbital in fact provides a pathway for ferromagnetic coupling which can compete with the antiferromagnetic pathway via $(\pi^{nb})_\sigma$. What is the physical nature of this CT excited state ferromagnetic interaction? As described in section IVA and IVB, the $(\pi^{nb})_\sigma(\pi^*)_\sigma$ ligand-excited configuration gives rise to the manifold of LE states which can be considered as deriving from a coupling of metal singlet and triplet configurations with ligand (excited) singlet and triplet configurations. From the interaction schemes Figures 14 and 16, we have seen that the dominant interaction in the case of mono(μ-1,1-azide) dimers is the interaction of the B_1 singlet and triplet CT states with the B_1 singlet and triplet LE states; for the bis μ-1,1 dimers, the analogous interactions are between the B_{1g} and B_{3u} singlet and triplet CT and LE states. For simplicity, we here only consider the mono(azide)-bridged systems with C_{2v} symmetry. Since the $(\pi^{nb})_\sigma$ and $(\pi^*)_\sigma$ orbitals have the same symmetry (b_1; cf. Figure 13), any ligand-excited configuration $(\pi^{nb})_\sigma(\pi^*)_\sigma$, singlet or triplet, transforms according to a_1. On the other hand, the metal singlet configuration

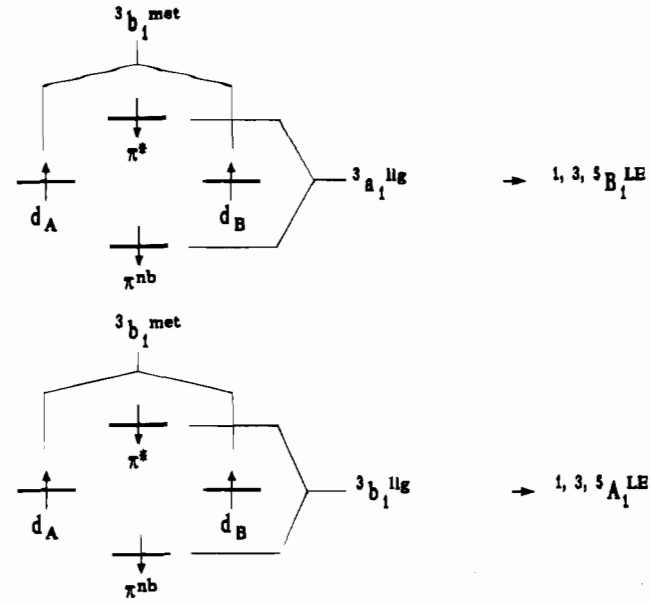

Figure 19. (a) Top: $M_S = 0$ LE configuration of symmetry B_1 deriving from coupling of a metal triplet and a ligand triplet (mono(μ-1,1-azido) dimers). (b) Bottom: $M_S = 0$ LE configuration of symmetry A_1 deriving from coupling of a metal triplet and a ligand triplet (cis μ-1,3-azide dimers).

transforms according to a_1 and the metal triplet configuration according to b_1. Hence, a LE state of B_1 symmetry must derive from coupling of a metal *triplet* $^3b_1{}^{met}$ with a ligand-excited singlet or triplet $^{1,3}a_1{}^{lig}$. Let us, e.g., consider the ligand-excited triplet. Figure 19 (top) displays the resulting $M_S = 0$ configuration, which appears in all states deriving from the coupling of the "local" triplets $^3b_1{}^{met} \times {}^3a_1{}^{lig} = {}^{1,3,5}{}_tB_1{}^{LE}$ (cf. Table 7). Importantly, $^1{}_tB_1{}^{LE}$ will interact with $^1B_1{}^{CT}$ and $^3{}_tB_1{}^{CT}$ with $^3B_1{}^{CT}$, leading to a shift of these CT states to lower energy (Figure 14). In particular, $^3B_1{}^{CT}$ will be lower than $^1A_1{}^{CT}$, which corresponds to a ferromagnetic contribution. The fact that the interaction between LE and CT states of B_1 symmetry is maximal (see Figures 14 and 17) is due to the possibility for the electron in the π^* orbital to delocalize toward the right *and* the left copper (corresponding to CT configurations) *without change of spin*. This can only be achieved if the spins in both Cu d orbitals are *parallel*, i.e. for a *metal triplet* configuration (Figure 19, top). The same reasoning can be applied to a singlet ligand-excited configuration with a spin-down electron in π^* (and a spin-up electron in $(\pi^{nb})_\sigma$) as long as the copper configuration is a triplet (this configuration, however, is not a singlet configuration and, hence, contributes only to a stabilization of the $^3B_1{}^{CT}$ state). Note that this ligand−metal delocalization corresponds to spin pairing in overlapping orbitals. In this sense, one can consider the metal system as "polarized" by the electron in the azide π^* orbital due to *simultaneous* spin-pairing of the Cu α spins with the β spin in the π^* orbital (or vice versa).

It is easily shown that the analogous mechanism leads to an antiferromagnetic interaction in the case of *cis*-μ-1,3-azide-bridged dimers. Since the $(\pi^{nb})_\sigma$ orbital now transforms according to b_1 and the $(\pi^*)_\sigma$ orbital according to a_1, the singlet and triplet $(\pi^{nb})_\sigma(\pi^*)_\sigma$ configurations transform according to b_1. In analogy to the above considerations, the largest CT−LE interaction occurs with LE states involving the metal triplet configuration transforming according to b_1, i.e. the LE states of $b_1 \times b_1 = A_1$ symmetry. The LE configuration deriving, e.g., from the metal *and* the ligand triplet configuration (Figure 19, bottom) occurs in all LE states of $^3b_1{}^{met} \times {}^3b_1{}^{lig} = {}^{1,3,5}{}_tA_1{}^{LE}$ symmetry. Importantly, the $^1{}_tA_1{}^{LE}$ state selectively lowers the

$^1A_1{}^{CT}$ state below $^3B_1{}^{CT}$ and, hence, gives an antiferromagnetic contribution which can be shown to be of the same magnitude as the ferromagnetic contribution in case of the μ-1,1 dimers. Whether the CT−LE interaction gives a ferro- or an antiferromagnetic contribution merely depends upon the symmetry of the ligand HOMO and LUMO (here for C_{2v}): if HOMO and LUMO are of the same symmetry (b_1), the LE states with the maximal CT−LE interaction have the same symmetry (B_1) as the *triplet* ground state and the interaction is ferromagnetic. If, on the other hand, HOMO and LUMO are of different symmetries (a_1 and b_1), the relevant LE states have the same symmetry (A_1) as the *singlet* ground state and the contribution is antiferromagnetic.

These considerations are closely related to the spin polarization model describing the ferromagnetism of the Cu(II) μ-1,1-azide dimers in terms of the four-electron spin Hamiltonian[15]

$$H = -2J_1(\mathbf{S}_A\mathbf{S}_C + \mathbf{S}_B\mathbf{S}_C) - 2J_2(\mathbf{S}_C\mathbf{S}_D) \qquad (21)$$

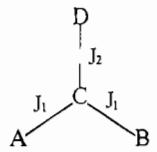

A and B refer to the two $S = {}^1/_2$ copper centers and C and D to the two terminal nitrogen atoms (C coordinating) of the bridging azide group where the two "active" ligand electrons are supposed to be located. Diagonalization of (21) shows that the μ-1,1 system is ferromagnetic for all values of J_1/J_2. For $J_1 \ll J_2$

$$2J^{GS} = E_{S=0} - E_{S=1} = 2J_1{}^2/(-2J_2) \quad (-2J_2 > 0) \qquad (22)$$

On the other hand, the VBCI model gives if the antiferromagnetic contribution is omitted (cf. (13), (11b))

$$2J^{GS} = W_{LE}^{GS} = \frac{2h_{d_A\pi}{}^2}{\Delta^2}\frac{2h_{d_A\pi^*}{}^2}{\langle\pi^*\rangle} \qquad (23)$$

With the energy of the ligand triplet $\langle\pi^*\rangle = -2J_2$, comparison of (22) and (23) leads to

$$J_1 = \frac{\sqrt{2}h_{d_A\pi}}{\Delta}h_{d_A\pi^*} \qquad (24)$$

For the cis μ-1,3 systems, diagonalization of the respective spin-Hamiltonian[15] in the same limit also leads to eqs 22 and 23, but now for $-2J^{GS}$, corresponding to an antiferromagnetic contribution of the same magnitude. Also (24) is equally valid. Thus, the spin polarization model is found to be a *spin-Hamiltonian description* of the CT−LE interaction, and the VBCI model provides values for the phenomenological constants J_1 and J_2 in terms of electronic structural parameters of the complex. In particular, J_1 corresponds to the copper d−azide π^* transfer integral scaled down by the GS−CT mixing coefficient $\sqrt{2}h_{d_A\pi}/\Delta$. A strong GS ferromagnetic interaction for the μ-1,1 and antiferromagnetic contribution for the cis μ-1,3 systems require good overlap between the metal d functions and *both* the occupied π and the unoccupied π^* orbital of the ligand. Of course, the antiferromagnetic interaction corresponding to conventional superexchange can be accounted for by an additional term $-2J_3\mathbf{S}_A\mathbf{S}_B$ in (21) (or in the respective spin-Hamiltonian for the cis μ-1,3 case[15]), a term $-2J_3$ in (22), and a term $-4h_{d_A\pi}{}^4/(\Delta^2U)$ in (23), where U denotes the energy of the metal → metal CT state (cf. (11) and (13)).

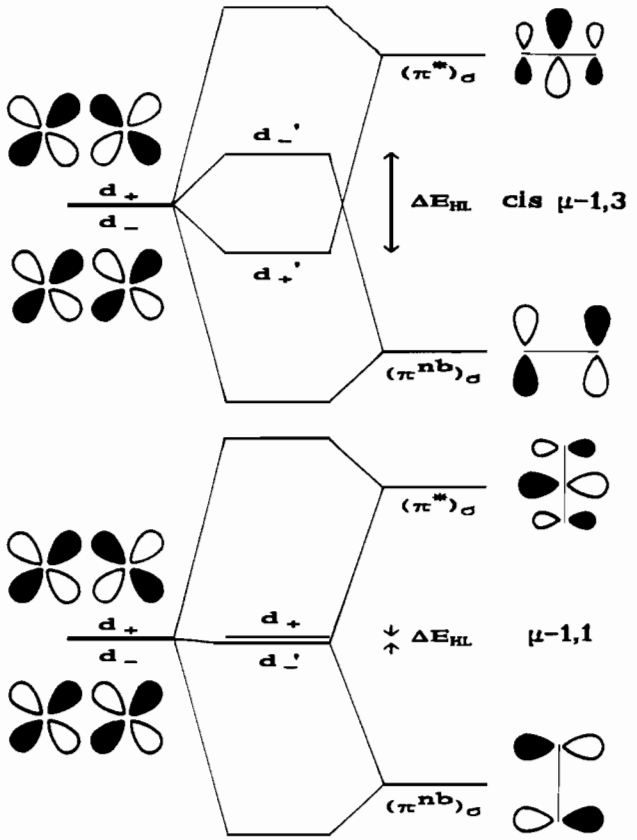

Figure 20. Interaction between the symmetric and antisymmetric combinations of Cu d_{xy} orbitals with azide HOMO $(\pi^{nb})_\sigma$ and LUMO $(\pi^*)_\sigma$: (a, top) μ-1,1-azido dimers; (b, bottom) cis μ-1,3 dimers.

Having seen how the spin polarization model can be understood by an interaction between the $^3B_1{}^{CT}$ and $^3{}_tB_1{}^{LE}$ states leading to a ferromagnetic contribution or the $^1A_1{}^{CT}$ and $^1{}_tA_1{}^{LE}$ states leading to an antiferromagnetic contribution, we can also make the connection to the molecular orbital description of magnetic exchange within the active electron approximation.[6a,23] As indicated before, the triplet azide → Cu CT state splitting $E(^3B_1{}^{CT}) - E(^3A_1{}^{CT})$ (for a system of C_{2v} symmetry) corresponds to the HOMO−LUMO gap ΔE_{HL}. Experimentally, this energy difference was determined to be -400 cm^{-1} for the tmen system, i.e. fairly small. (For the tbupy system of D_{2h} symmetry, ΔE_{HL} is given by $E(^3B_{3u}{}^{CT}) - E(^3A_g{}^{CT})$.) On the other hand, the calculated value of the triplet CT state splitting and the HOMO−LUMO gap for the *cis*-μ-1,3-azide-bridged dimer was large (6850 cm^{-1} [20]). This difference is qualitatively understandable from the orbital symmetries of the ligand and metal HOMO's and LUMO's (Figure 20): whereas for the cis μ-1,3 case the ligand $(\pi^{nb})_\sigma$ and $(\pi^*)_\sigma$ orbitals both act to increase ΔE_{HL} (Figure 20, top), they act against each other in the case of μ-1,1-bridged dimers, making ΔE_{HL} small if both interactions are of comparable magnitude (Figure 20, bottom). These interactions correspond to "backbonding" of the azide group. Qualitatively, the influence of the azide $(\pi^{nb})_\sigma$ and $(\pi^*)_\sigma$ orbitals drives the μ-1,1-bridged system toward accidental degeneracy of the HOMO and the LUMO which, in terms of the "active electron approximation", is the condition for ferromagnetic coupling. Note, however, that in terms of the VBCI model not $\Delta E_{HL} = E(^3B_1{}^{CT}) - E(^3A_1{}^{CT}) \approx 0$ but $2J^{CT} = E(^1A_1{}^{CT}) - E(^3B_1{}^{CT}) > 0$ is a necessary condition for ferromagnetic coupling.

Finally, the azide → Cu CT spectra show for both the mono μ-1,1 and the bis μ-1,1 dimers clear evidence for progressions in the asymmetric azide stretching mode. The measured excited state frequency (2400−2700 cm^{-1}) is 15−30% larger than the

ground state frequency (~2100 cm^{-1}) measured by Raman spectroscopy for both the tmen and the tbupy system.[28] We assume that the main effect leading to this increase of the stretching frequency is the removal of one electron from the azide HOMO, leading to an even stronger asymmetry in the N−N bond lengths than in the ground state.[8,9,33] In one particular case, the C band in the tbupy dimer, one progression is fully observable and allows us to probe the excited state potential. The strong deviation from harmonicity in both spacings and intensities is interpreted as arising from vibronic coupling with another CT state ~7500 cm^{-1} higher in energy. In the case of the other CT transitions, in particular the singlet → singlet transitions, the information is less complete. The intensity distribution also strongly deviates from harmonic behavior, in particular in case of band B of the tbupy system, which is again an indication for the presence of vibronic interactions between these CT states.

In summary, the present study has demonstrated how the ligand → metal CT excited state structure can be used to obtain information about magnetic exchange pathways in ferromagnetically coupled dimers. It has been experimentally shown that the antiferromagnetic interactions in the CT states corresponding to superexchange are compensated by a ferromagnetic interaction of comparable magnitude. The origin of this ferromagnetic interaction has been assumed to lie in a $(\pi^{nb})_\sigma$-$(\pi^*)_\sigma$ ligand-excited configuration which in the case of mono-(μ-1,1-azide)-bridged dimers selectively stabilizes B_1 states and in the case of bis μ-1,1 dimers B_{1g} and B_{3u} states. On the basis of this model, the CT spectrum has been successfully parametrized, giving about equal values for the transfer matrix elements between the d orbitals and $(\pi^{nb})_\sigma$ and $(\pi^*)_\sigma$, respectively. Further, the correspondence between this concept and the spin polarization model has been demonstrated, and it has been shown that the π^* orbital acts to decrease the HOMO−LUMO gap, driving the μ-1,1-azide-bridged systems toward accidental degeneracy. Hence, the question of whether the ferromagnetism of the μ-1,1-azide-bridged dimers is due to the spin polarization model or accidental degeneracy is meaningless since both concepts are qualitatively (not quantitatively) descriptions of the same mechanism, spin polarization in a VB and accidental degeneracy in a MO framework. The VB description, however, makes clear that the pathway over the unoccupied π^* orbital should potentially provide a very strong ferromagnetic pathway if the π^* orbital is at sufficiently low energy. This should be tested on a larger class of dimers with suitable bridging ligands.

Acknowledgment. F.T. thanks the Fonds der Chemischen Industrie for support of this research.

(33) Archibald, T. W.; Sabin, J. R. *J. Chem. Phys.* **1971**, *55*, 1821.

IC950295V